UNIVERSITY OF TWENTE.

Mechanical Engineering
Engineering Fluid Dynamics

Building a test setup for pulsed laser ablation in liquid flow

Master thesis

ing. P.J. Stöver

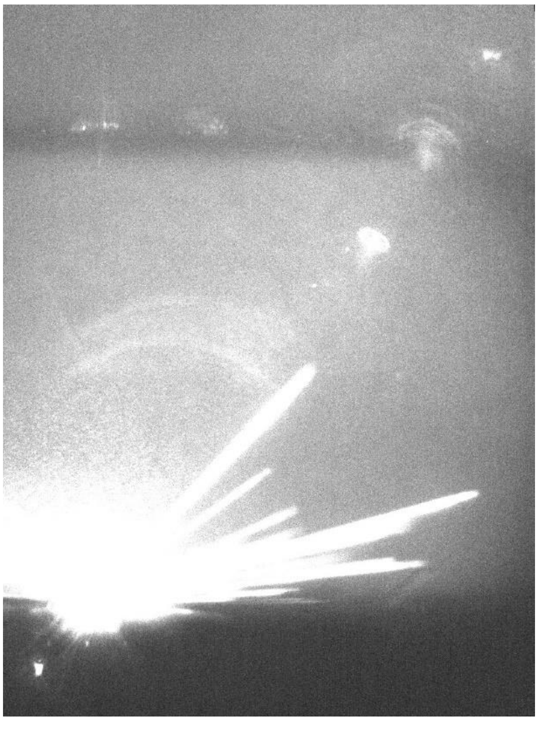

Graduation Committee:

dr. ir. R.Hagmeijer	prof. dr. ir. G.R.B.E.Römer
ir. S. Van der Linden	dr.ir. R.G.K.M Aarts

Enschede, June 2021

372

Summary

The goal of this report is to create a test setup that can create predictable and repeatable flow conditions to facilitate nanosecond pulsed laser ablation in a liquid flow. Literature is reviewed to understand what parameters influence the ablation process and what flow setups were used in prior research. Based on these findings a set of two main design prerequisites is determined: the flow should have a known velocity profile and the design should allow for imaging of the ablation process. The former prerequisite was fulfilled by creating a channel with a 5x$25mm$ internal cross-section and a $543mm$ hydraulic entrance length. This design can sustain a fully developed laminar flow up to a Reynolds number of 2000. Over a width of $10mm$, the velocity profile can be considered a 99% approximation of a 2D flow. The latter prerequisite is fulfilled by allowing a long distance 50x magnification lens to image within the region of approximate 2D flow. The channel features a sample rotation mechanism that allows for a fixed alignment of the camera with the laser, while the sample can be rotated for a new crater spot. So the camera needs to be focused only once.

PIV-measurements, in the Reynolds range of 13 to 11721 are performed to verify the theoretical velocity profile and to investigate the transition to turbulent flow. The flow is created with a pneumatic cylinder. Pictures of the $40-70\mu m$ tracer particles are taken with an SX9M camera over the entirety of the stroke of the cylinder. A formula is created to select the right frames for when the flow is fully developed: fully developed flow requires that the liquid passes the hydraulic entrance length before becoming fully developed. The PIV-measurements show that the theoretical profile can indeed be reproduced up to a Reynolds number of 1952. For higher flow rates, the profile starts to deviate from its fully developed parabolic shape and becomes more rectangular.

After the verification of the velocity profile, the channel is mounted on the xy-stages of the laser system. An Arduino micro-controller is used to enable the communication between laser control system, the hydraulic system and the sample rotation system. The integration with an Arduino allows a significant part of the laser experiment to be automated. After aligning the laser and setting the focus on the sample in the channel, ablation experiments are conducted with three different pulse frequencies ($100Hz$, $1kHz$ and $10kHz$), 4 pulse energies ($0.155mJ$, $0.166mJ$, $0.177mJ$ and $0.188mJ$) and 4 Reynolds numbers (0, 13, 1953 and 6512). Both cavitation bubbles and persistent bubbles are imaged both, verifying that the integration of the channel with the laser system is successful. Imaging of the interaction of persistent bubbles with the liquid flow is not possible due to the high number of bubbles that are introduced in the flow by the hydraulic system.

For a fully functional test-setup the introduction of bubbles by the hydraulic system should be investigated and prevented to make sure that the bubbles introduced in the channel are only created by the laser process. The PIV-measurements can be improved by increasing the lighting conditions and the use of better trace particles. This would allow a more accurate determination of the transition of the laminar flow regime to a turbulent flow. A high speed camera should be used to image the dynamic behaviour of the persistent bubbles with the liquid flow in a follow-up research. This would allow the visualisation of the bubble trajectory as it is influenced by the flow.

Contents

Chapter 1

Introduction

Short, high power laser pulses can be used to remove material by breaking the electron bonds of the base material. The laser pulses creates a highly ionized plasma due to the breakage of these electron bonds. The ionized plasma is then repelled by the base material, leaving a crater at the interaction zone of the laser and base material. The laser pulse duration is so short that there is a minimal introduction of heat in the material. Additionally, melting or vaporization take no part in material removal. This unique way of removing material is called laser ablation. Laser ablation as a machining process has the advantage that there is (almost) no heat affected zone. Randomness of melting and recrystallization are not present, which is beneficial for the repeatability and precision of the machining process.

Laser ablation can also be performed under a liquid layer. Pulsed Laser Ablation under Liquid (PLAL) has an increased effectiveness in terms of material removal rate and precision over ablation in a gas or vacuum for many cases due to the confinement of energy of the laser pulse by the liquid layer, the reduction of the heat affected zone and prevention of re-deposition of ablated material. The material removal rate is improved because the ablation phenomena are confined by a liquid layer. Ablation phenomena are the plasma plume, cavitation bubble and shockwave that are created by the laser material interaction. Figure 1.1 shows a rendered representation of the ablation phenomena placed on a time scale to show how the ablation develops over time. The ablation phenomena and their influencing factors are reviewed in the first paragraph of the next chapter. In-situ ablation analysis methods are also examined in paragraph three.

Typical laser ablation systems have a pulse frequency of at least $1kHz$. Persistent bubbles exist on the same, or longer time scale. Persistent bubbles can refract the incoming laser light and can prevent the laser light from reaching its intended destination. An example of this effect can be seen in figure 1.2 ((a) and (b)). A liquid flow can drag these obstructions away from the laser spot. Systems with flowing liquid have been introduced and researched already. The effectiveness of dragging the obstructions along with the flow is shown in figure 1.2 (c). There are several methods of introducing a flow. An overview of these existing methods is given in paragraph two in the next chapter.

From this overview it becomes clear that research on the flow properties such as the Reynolds number or velocity profile in combination with laser ablation was never done before. This study will therefore focus on creating a liquid flow with known flow properties. The goal of this study is thus: to create a test setup that can produce predictable and repeatable flow conditions that allow the research of the interaction of the ablation phenomena with a liquid flow. In chapter three, the test setup will be designed based on these literature findings, making sure that the channel has a well-defined velocity profile with adequate optical access for the in-situ ablation analysis method. A method for rotating the sample, that ensures that the camera remains focused on the laser spot, is introduced in paragraph four. Chapter three ends with an overview of the components that are used for imaging the ablation event and sample rotation.

The velocity profile in the test setup is then validated by particle image velocimetry (PIV) for laminar and turbulent flows in chapter four. The hydraulic system that is used to create the flow, is introduced

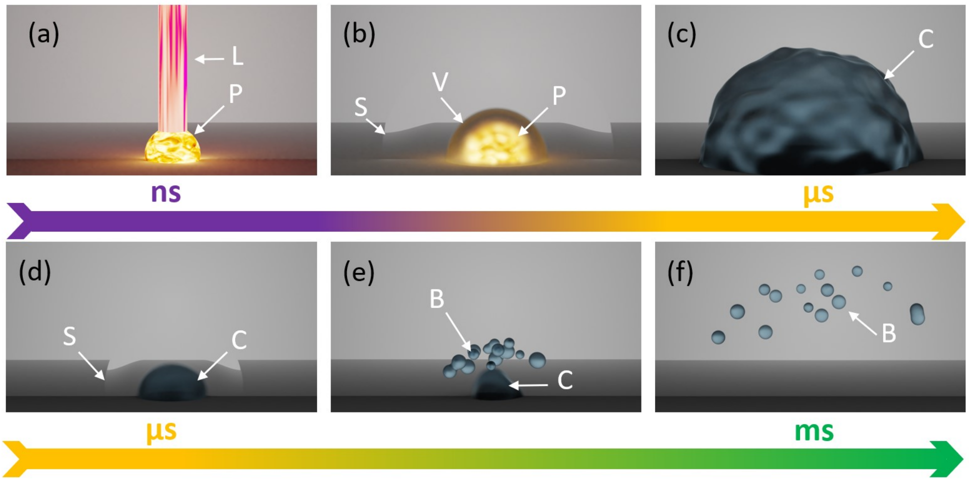

Figure 1.1: This figure shows the sequence of ablation phenomena. The rendered images are placed on a time scale to roughly indicate when events take place. (a) the laser (L) interacts with the base material and creates a plasma (P). (b) the plasma heats up the liquid and creates a small vapor layer (V) around it. A shockwave (S) is created by the rapid expansion of the liquid. (c) the vapour layer expands into a cavitation bubble (C). (d) the cavitation bubble collapses, rebounds and sends out another shockwave. (e) after the collapse of the rebounded cavitation bubble, persistent bubbles (B) are expelled. (f) persistent bubbles remain present in the fluid for several milliseconds up to several seconds.

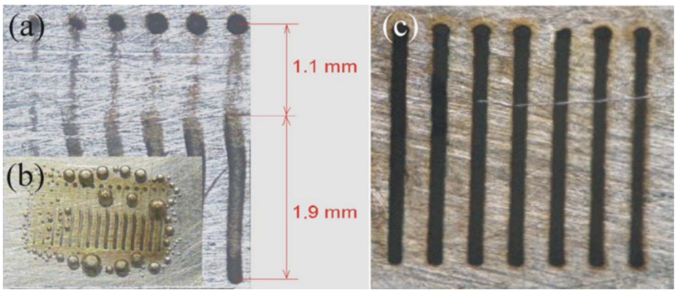

Figure 1.2: PLAL of a straight line in stagnant water ((a) and (b)) with the pressence of persistent bubbles. (c) straight lines as the persistent bubbles are removed with a water flow. [1]

in the first paragraph of this chapter. The lighting, camera and software that are used for the PIV test specifically, are covered in the subsequent paragraphs. A large data set of analyzed PIV measurements for a Reynolds number up to 11721 is created and analyzed. As the PIV measurements are performed three times per Reynolds number, the measurements are grouped and averaged per Reynolds number. In the last paragraph, the results are plotted in a single figure to show how the laminar flow transitions to turbulent flow.

After the flow validation, the test setup is integrated on the optical table in chapter five to do some preliminary test on the interaction of the laser created persistent bubbles and a liquid flow. An Arduino micro-controller is used to communicate with the laser computer, in order to sync the laser pulses with the flow conditions and to rotate the sample after a crater is shot. A trigger system that counts the number of laser pulses and triggers the camera and LED to take a photo of the persistent bubble, is also explained in this chapter. In the last two paragraphs, the test procedure is explained and the test results are presented. In the final chapter, the conclusions of this report are presented together with some recommendations on future improvements of the test setup.

Chapter 2

Literature review

The literature is studied in three main areas: ablation phenomena, existing flow setups and imaging techniques. As the test setup will be used to study the ablation phenomena it is important to understand how the design of the channel can influence the ablation parameters. Existing flow setups are studied in order to understand what kind of setups were made already and how these setups were used to study the interaction of a liquid flow with the ablation process. Finally, some imaging techniques that are frequently used to image the ablation phenomena are reviewed. These techniques will give insight in how the test setup should be designed such that the ablation phenomena can be accurately imaged.

2.1 Ablation phenomena and their influencing parameters

The ablation process starts with the laser material interaction that causes electron excitation, lattice heating and lattice disintegration [2]. The disintegrated ions and electrons from the lattice form a plasma above the ablation spot. The plasma interacts with the confining liquid layer creating a shockwave and forms a cavitation bubble in the liquid. At the collapse of the cavitation bubble a second shockwave is emitted and persistent bubbles can be created [3]. The time scale of the electron excitation and lattice disintegration is so short (a few ps to $100ps$) that interaction with a flowing liquid is negligible and will not be considered in the design of the test setup. On the other hand, the properties of the plasma, cavitation bubbles, shock waves and persistent bubbles have been shown to be dependent on the liquid properties.

An ablation plasma behaves quite differently in a liquid than in air, expanding much slower and expanding less in a liquid [4]. The fluence threshold is reduced and the ablation efficiency is increased by confining the plasma with a liquid [5]. Plasma expansion was imaged in different liquid types and investigated for their ablation effectiveness showing that the material removal rate in water is higher than in methanol, acetone, ethanol and toluene [6]. Static liquid pressure does not seem to change the shape of the plasma plume a lot but does have a dominant effect on the cavitation bubble [7]. Plasma plumes are known to shield incoming laser light and reduce the mass that is ablated per pulse [8]. A plasma plume has not been imaged in the presence of a liquid flow, although a suggestion has been made how a liquid flow interacts with the plasma plume and how it can enhance the effectiveness of the ablation process. This is done by pushing the shielding plasma plume to the side, shown schematically in figure 2.1 [9].

The plasma plume causes a cavitation bubble and shockwave to form on the interface with the water and the plasma. The shockwave has an initial speed of $2600m/s$ that later reduces to $1500-1600m/s$, roughly the speed of sound in water [10]. The shockwave speed seems to match the speed of sound of liquids like acetone ($1200m/s$ [11], toluene ($1400m/s$ [11]) and water ($1500m/s$ [12]). The size of the cavitation bubble is dependent on the pulse energy; more energy yields a bigger bubble [13]. Table 2.1 gives an overview of the size of the cavitation bubble in relation to the pulse energy. After reaching its maximum size the, cavitation bubble collapses and rebounds into a second bubble that is smaller

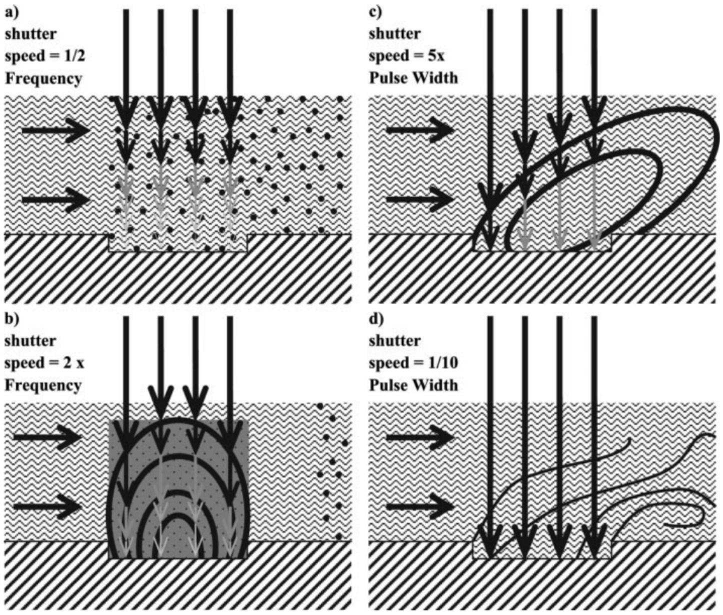

Figure 2.1: Dowding: "Schematic showing flow–plume interaction states when: (a) the flow rate is laminar and the laser pulse frequency is high, thus the following pulse is intercepted by remaining suspended debris; (b) increased flow velocity beneath the optimum allows the ablation plume to fully develop, maximizing plume attenuation while compensating by uninhibited plume etching; (c) an optimum condition occurs when the flowing liquid distorts the ablation plume to minimize plume attenuation without removing the action of plume etching; (d) very high flow velocity with respect to the pulse width results in distortion of the ablation plume by the viscous fluid" [9]

[14] [15]. At the collapse of the first bubble a second shockwave is observed. Like for the plasma, the properties of the cavitation bubble are influenced by the type of liquid and the liquid pressure [16] [17] [18]. High pressures ($> 3 \cdot 10^6 Pa$) reduce the lifetime of cavitation bubbles and prevent a rebound and emission of a second shockwave, after the collapse of the first cavitation bubble [19]. At an even higher pressure ($> 3 \cdot 10^7 Pa$) the extinction process is the same (no second bubble), but a third shockwave is observed [19]. The way the ablation target is fixated also influences the cavitation bubble dynamics; a wire target clamped on one end or on both ends shows a bigger cavitation bubble volume than a bulk target [20].

The liquid layer height, that is the height of the water above the sample, also has an influence on the size and shape of the cavitation bubble [21] [22]. The liquid layer height is not only important for the size of the cavitation bubble it also has a big influence on the overall ablation process. The material removal rate per pulse is most effective with a liquid layer height of $1mm$ [23] [24] [25]. On the collapse of cavitation bubbles, persistent bubbles can be created that can persist for several seconds [3]. These persistent bubbles can diffract the incoming laser light and disrupt the ablation process by scattering the laser light [26]. Additionally, the cavitation bubbles can exist long enough to shield the target from incoming laser light if the pulse frequency is high enough [27].

2.2 Existing flow setups

A liquid flow can remove the shielding nano-particles and persistent bubbles from the laser interaction zone. An overview of different flow enabling methods found in literature is given in figure 2.2.

Setup (a) and (b) were used to determine the influence of the laser traverse speed, laser pulse energy and the water flow rate on the quality, depth and width of a groove cut in silicon (a) [28] and

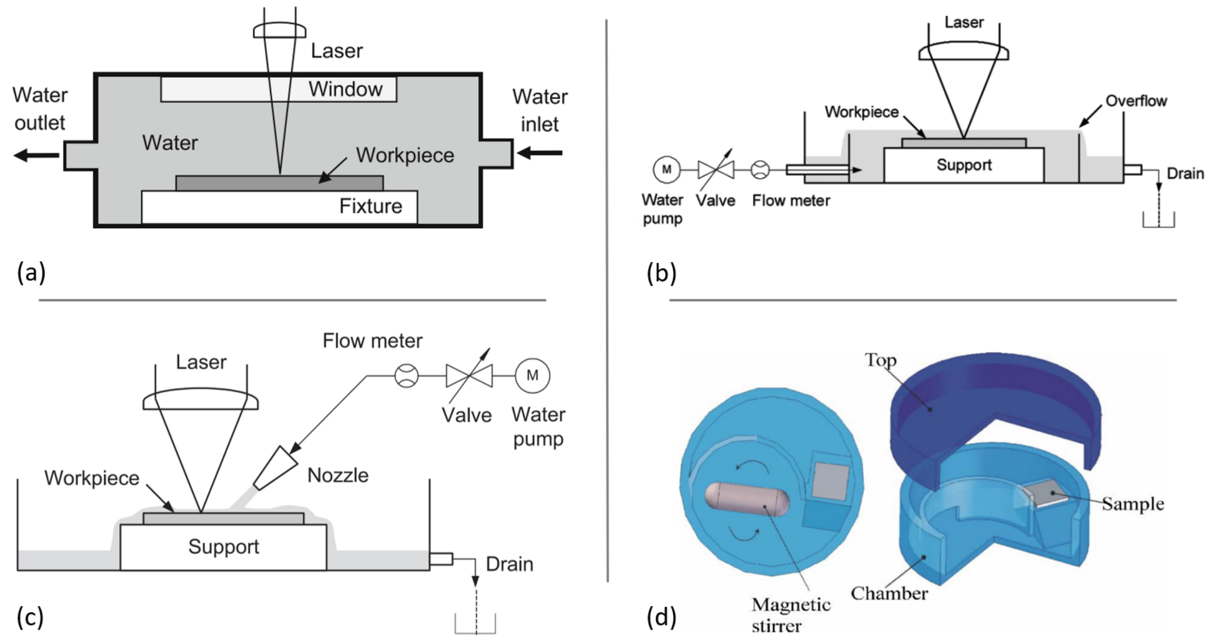

Figure 2.2: (a) A design of a closed chamber with a glass for the laser and camera from the side [28]. (b) An overflow system [29]. (c) An open system with a water flow introduced by a nozzle from the side [30], (d) A closed chamber design with a stirr-bar for flow circulation [26]

titanium (b) [29] with a Nd:YAG laser. Setup (a) was used in a subsequent study to image the dynamic behaviour of cavitation bubbles in a flow [31]. Setup (c) is an adaptation of a hybrid laser system where the laser travels through the water to the workpiece. An example of a co-axial hybrid continuous laser and water system is used as a paint remover [32]. Usually these hybrid systems are mechanically complex since the water needs to be ejected co-axially from the same nozzle as the laser. Setup (c) circumvents this problem by locating the water nozzle of axis. The nozzle can now be positioned independently from the laser, allowing the distance and angle to be adjusted compared to the laser. The flow characteristics of this setup were analyzed numerically and experimentally, showing that the angle of the nozzle has a big impact on the pressures and speeds of the flow [33]. The same setup was used to determine that the liquid flow direction should be aligned with the laser direction to get the most uniform and smooth surface [33]. Setup (d) was created to improve the production of nanoparticles by creating a flow with a stir bar in order to remove the bubbles formed at the surface. The system used in figure 2.1 is a closed chamber system (a) that is used a precise flow measurement to accurately determine the Reynolds number. It showed that an increase in flow velocity can increase the ablation rate [9].

2.3 Imaging techniques

The development of the plasma plume and shockwave can be monitored acoustically [5] [8], but the use of imaging techniques like shadowgraphy also allow the monitoring of cavitation bubble and persistent bubbles. Adaptation to the shadowgraphy technique are also used in the field of laser ablation: a photo-elasticity imaging technique allows the imaging of stress waves induced by the plasma and cavitation bubbles by polarizing the back light, giving an indirect indication of the induced stress by the amount of fringes that are visible on the image [34] [35]. A high-speed two frame shadowgraphy imaging technique is demonstrated that allows the imaging of the high speed expansion of the plasma $(100-600km/s)$, by taking pictures with two cameras with a minimum of $300ps$ between frames [36]. To do high-speed imaging in fluids, three basic parameters have to be considered [37]: the cameras frame rate, the image magnification and exposure time. These parameters are all depending on the speed and size of the process to be imaged and their requirements increase when the process becomes spatially and temporally shorter. An overview of sizes and duration of the cavitation bubbles found in literature are listed in table 2.1. The first four columns show the properties of the laser pulse. The 'Remarks' column shows if the ablation took place in something other than water at ambient pressure. For more detail of the ablation parameters, refer to the source.

Laser source	Wavelength	Pulse Duration	Pulse Energy	Bubble Radius	Duration	Remarks	Source
Nd:YAG	$532nm$	$8ns$	$30mJ$	$2mm$	$350\mu s$	In water ablation, no target	[38]
Nd:YAG	$1064nm$		$125mJ$	$7mm$	$600\mu s$	Isopropanol	[16]
Nd:Glass	$527nm$	$250fs$	$3mJ$	$0.45mm$	$100\mu s$	Aceton	[39]
Nd:YAG	$1064nm$	$8ns$	$20mJ$	$1mm$	$180\mu s$		[40]
Nd:YAG	$1064nm$	$13ns$	$20mJ$	$2.7mm$	$380\mu s$		[22]
Nd:YAG	$1064nm$	$10ns$	$32.8mJ$	$2.22mm$	$333\mu s$	Elevated water temperature	[41]
Nd:YAG	$1064nm$	$8ns$	$0.35mJ$	$1.4mm$	-	Isopropanol	[3]
Nd:YAG	$1064nm$	$10ns$	$22mJ$	$1mm$	$185\mu s$	Ambient pressure	[19]
Nd:YAG	$1064nm$	$10ns$	$22mJ$	$0.25mm$	$10\mu s$	300bar	[19]
Nd:YAG	$1064nm$	$13ns$	$50mJ$	$1.4mm$	$280\mu s$		[12]
Nd:YAG	$1064nm$	$13ns$	$100mJ$	$2.2mm$	$400\mu s$		[12]
Nd:YAG	$1064nm$	$10ns$	$6mJ$	$2.8mm$	$200\mu s$		[13]
Nd:YAG	$1064nm$	$10ns$	$12mJ$	$4mm$	$300\mu s$		[13]
Nd:YAG	$1064nm$	$10ns$	$10mJ$	$1.5mm$	$300\mu s$	Thin wire target	[20]
Nd:YAG	$1064nm$	$120ns$	$0.5mJ$	$0.13mm$	$60\mu s$	Water flow	[31]

Table 2.1: A table with cavitation bubble radii and pulse energies found in literature mainly for Nd:YAG lasers (similar to the laser used in this study).

The values of table 2.1 are plotted in figure 2.3. A linear line is fitted and it shows a moderate relation between the pulse energy and cavitation bubble size ($R^2 = 0.42$). Much less is know about the size and duration of the plasma in water. One example shows that with a pulse energy of $60mJ$, a $100\mu m$ plasma plume can be created for $57\mu s$ in water [4]. Based on the overview in table 2.1 and linear fit in figure 2.3 a rough estimation can be made on the expected size and duration of the cavitation bubble for the pulse energy from the laser that will be used with this test setup. A design for the imaging system can be made accordingly. It is difficult to make an estimation of the size and duration of the plasma plume based on a single example. A optical system could be designed if more was known about the plasma plume.

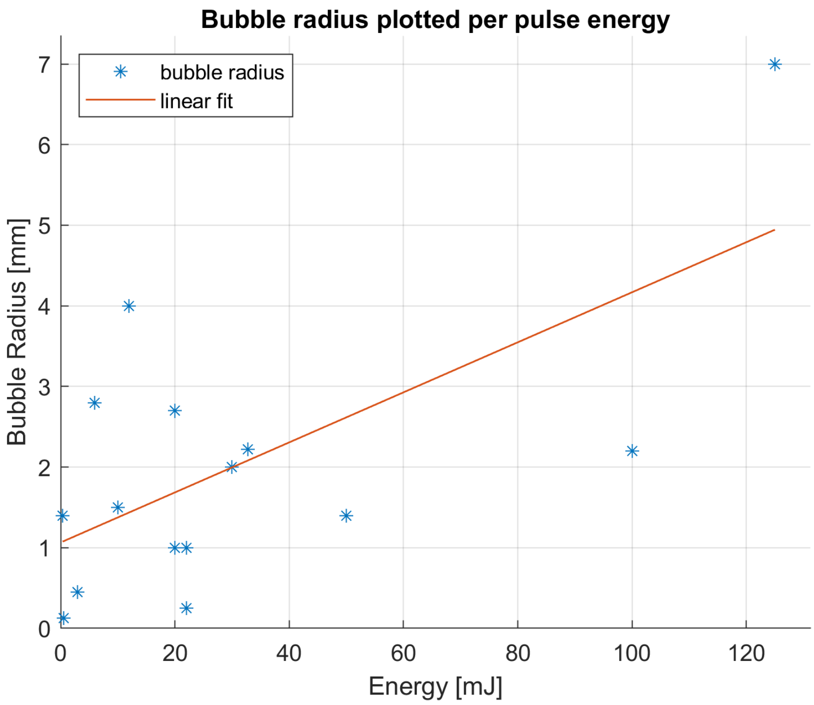

Figure 2.3: Cavitation bubble radius vs. pulse energy. Data from table 2.1. The linear fit of the data, with an $R^2 = 0.42$, shows a moderate relationship between the pulse energy and cavitation radius

Chapter 3

Design

This chapter discusses the design of the test setup. First, the design prerequisites are determined based on the results of the literature review. The design requirements from these consideration are incorporated in a design for fully developed flow and optical access to the ablation process. Then, a mechanical design for mounting a sample is covered and sample preparation is explained. The chapter ends with an overview of the design of the test setup and how it will be used in the PIV- and laser tests.

3.1 Design considerations

The goal in this report is to design a test setup for a liquid flow ablation process. Examples of different kinds of setups were found in the literature (figure 2.2). Most of these setups lack an indication of local velocities or a Reynolds number. The velocity field of setup (c) has been investigated numerically and experimentally [33]. The Reynolds number of a setup (a) type was also known [9]. Unfortunately, setup (c) does not allow easy optical access to the ablation process without disturbing the flow conditions too much as any optical glass placed in the flow would interrupt the flow itself.

A fully developed flow has a known velocity profile that is analytically determined for closed channels for many different cross-sections [42]. There are two ways to verify if a flow has become a fully developed flow. The center line velocity has reached 99% of its maximum velocity ($u \geq 0.99u_{max}$). Or, the pressure drop in stream-wise direction has become constant ($dp/dx = constant$). A known, well-defined velocity profile can be beneficial for the understanding of the interaction between the ablation process and a liquid flow, and will therefore be the basis of the test setup presented in this report.

Literature shows that the ablation process can be monitored acoustically, but it is usually and more frequently monitored with cameras. A camera can be used to monitor less acoustic events (less acoustic than a shockwave or cavitation bubbles) such as the persistent bubbles. The ablation phenomena are quite fast and quite small, requiring fast cameras and short exposure times to image them. High magnification lenses are needed to capture the small plasma plumes, cavitation bubbles and persistent bubbles. These lenses should have adequate optical access (close proximity to the ablation events) and the test setup should be designed accordingly. Crater analysis is another tool that is frequently used to study the effects of different parameters on the ablation process. One such parameter is sample material type. The test setup should allow the uses of different sample material types, that can be fitted under a microscope for crater analysis. Pulse energy, pulse frequency, pulse duration, spot size and laser focus distance can all be chosen independent of the setup design and are determined by the capabilities of the laser and optical equipment in the lab (see table 5.1 for the laser).

Liquid layer height is an important factor in the ablation efficiency and should ideally be set to $1mm$ when the liquid is stagnant. Creating a closed-chamber design with an adjustable liquid layer height to determine how a liquid flow would affect the ideal liquid layer height would make the design quite complex. Therefore the design will have a fixed layer height to reduce design complexity. The height will be set to 5mm to prevent cavitation shockwave damage to the setup. To further reduce complexity, another parameter that is omitted from the design considerations is liquid pressure. The test setup will initially be filled with demineralized water. the liquid type can later be altered if the liquid is compatible with the materials in the channel (it should not, for example, dissolve glues and coatings).

3.2 Velocity profile

A rectangular cross-section was chosen for the channel design. This type of cross-section allows the camera and laser to be mounted perpendicular to each other (see figure 3.1).

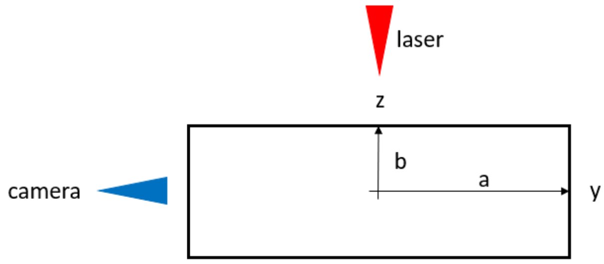

Figure 3.1: The cross-section of channel. The origin lies at the center. The flow direction is perpendicular to the yz-plane.

$$u(y,z) = \frac{16a^2}{\mu\pi^3}\left(-\frac{dp}{dx}\right)\sum_{i=1,3,5,\ldots}^{\infty}(-1)^{(i-1)/2}\left[1-\frac{cosh(i\pi z/2a)}{cosh(i\pi b/2a)}\right]\frac{cos(i\pi y/2a)}{i^3} \tag{3.1}$$

$$Q = \frac{4ba^3}{3\mu}\left(-\frac{dp}{dx}\right)\left[1-\frac{192a}{\pi^5 b}\sum_{i=1,3,5,\ldots}^{\infty}\frac{tanh(i\pi b/2a)}{i^5}\right] \tag{3.2}$$

$$u_{2D}(z) = \frac{1}{2\mu}\left(\frac{dp}{dx}-\rho g\right)(z^2-b^2) \tag{3.3}$$

$$\tilde{u}_{12.5mm} = \frac{u_{12.5mm}}{max(u_{2D})}, \quad \tilde{u}_{25mm} = \frac{u_{25mm}}{max(u_{2D})}, \quad \tilde{u}_{2D} = \frac{u_{2D}}{max(u_{2D})} \tag{3.4}$$

The 3D-velocity profile and flow rate (Q) of a fully developed flow for a rectangular cross-section can be calculated with equation 3.1 and 3.2 respectively [42], where a en b are defined as in figure 3.1. Dimension $b = 2.5mm$ half the liquid layer thickness. Dimension a is constrained by the available glass-dimensions from Edmund optics (a supplier for optical glass): $12.5mm$, $25mm$ and $50mm$. The 3D velocity profile for both $2a = 12.5mm$ and $2a = 25mm$ are plotted in figure 3.2 and 3.3. The red line in both plots indicates the velocity in the xy-plane which are plotted on the right in their respective figures. The velocity profile in the xy-plane for the two channel widths are normalized by the 2D velocity profile (equation 3.3 in equation 3.4. They are then plotted together in figure 3.4, to emphasise that for a smaller ratio of b/a a 2D flow is approximated.

$$\frac{\partial u}{\partial y}(y,z) = \frac{16a^2}{\mu\pi^3}\left(-\frac{dp}{dx}\right)\sum_{i=1,3,5,\ldots}^{\infty}(-1)^{(i-1)/2}\left[1-\frac{cosh(i\pi z/2a)}{cosh(i\pi b/2a)}\right]\frac{-\pi sin(i\pi y/2a)}{2ai^2} \tag{3.5}$$

$$\frac{\partial^2 u}{\partial y^2}(y,z) = \frac{16a^2}{\mu\pi^3}\left(-\frac{dp}{dx}\right)\sum_{i=1,3,5,\ldots}^{\infty}(-1)^{(i-1)/2}\left[1-\frac{cosh(i\pi z/2a)}{cosh(i\pi b/2a)}\right]\frac{-\pi^2 cos(i\pi y/2a)}{4a^2 i} \tag{3.6}$$

To show how the 3D velocity profile approximates the 2D profile for smaller ratios of b/a, the derivative of equation 3.1 with respect to y is taken in equation 3.5. The outcome is normalized and plotted for two ratios in figure 3.5 (a). As expected, the change in velocity in the y-direction reduces for smaller

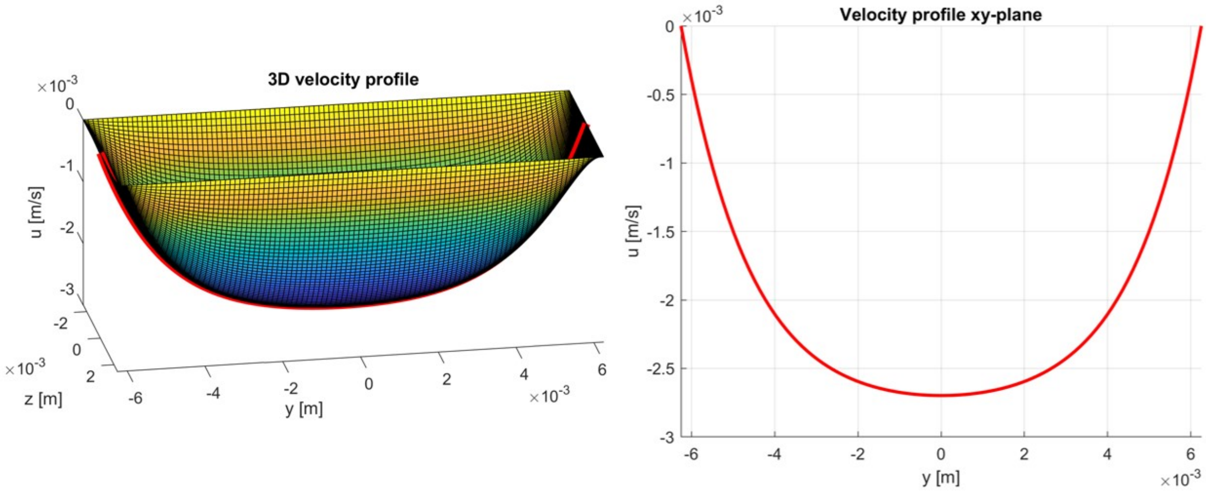

Figure 3.2: A 3D velocity profile for channel width of $12.5mm$ with a cross-section at the xy-plane.

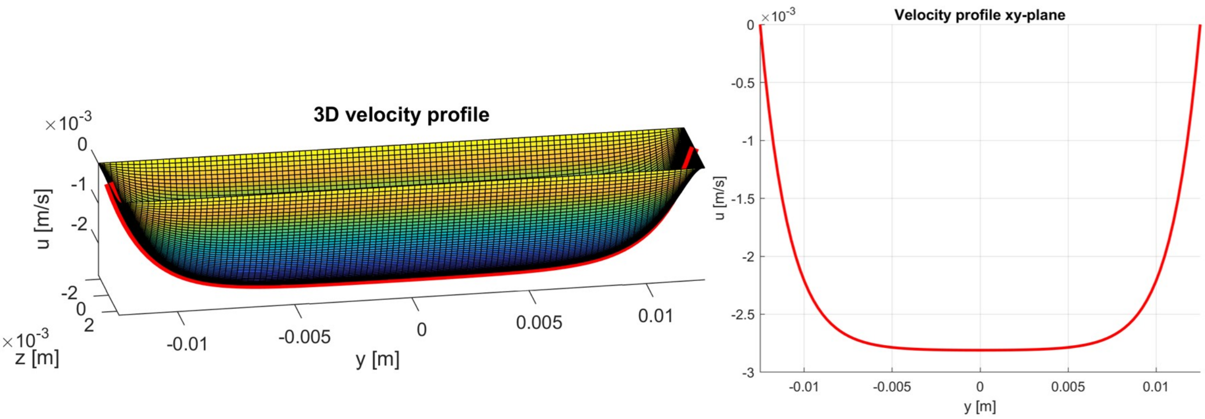

Figure 3.3: A 3D velocity profile for channel width of $25mm$ with a cross-section at the xy-plane.

ratios of b/a, indicated by the reduction in slope around $\tilde{a} = 0$ (non-dimensionalized width). If the slope of equation 3.5 at $\tilde{a} = 0$ approaches zero, the profile becomes two dimensional. The second derivative with respect to y is taken in equation 3.6, to calculate the the slope of the first derivative. The plot of the normalized derivative shows how it approaches zero for smaller ratios of b/a in figure 3.5. In figure 3.5 (b), the difference of the normalized 2D velocity profile and 3D profile is also added. The difference between the two also becomes zero for smaller ratios of b/a.

3.3 Optical access

The ablation process should be optical accessible for imaging purposes. This means that high magnification microscopes, which are needed to image the small processes like the plasma plume and cavitation bubble, should be mountable close to the laser focus. Based on the literature on cavitation bubbles (see table 2.1) and on the pulse energy of the laser used with this setup (see table 5.1), the expected diameter of the cavitation bubble is $100\mu m$. That means that for a full size image of a cavitation bubble, a lens with a magnification of 50x is needed for the available camera. Figure 3.6 shows the difference in optical access for the two different dimensions of a (the width) for two Mitutoyo long working distance objectives. The black square on the right represents the Silica window with a refractive index of $n = 1.462$ [43]. To calculate the rest of the optical paths, a refractive index of $n = 1.330$ for water is used. Figure 3.6 shows that optical access with a high magnification objective to an area where

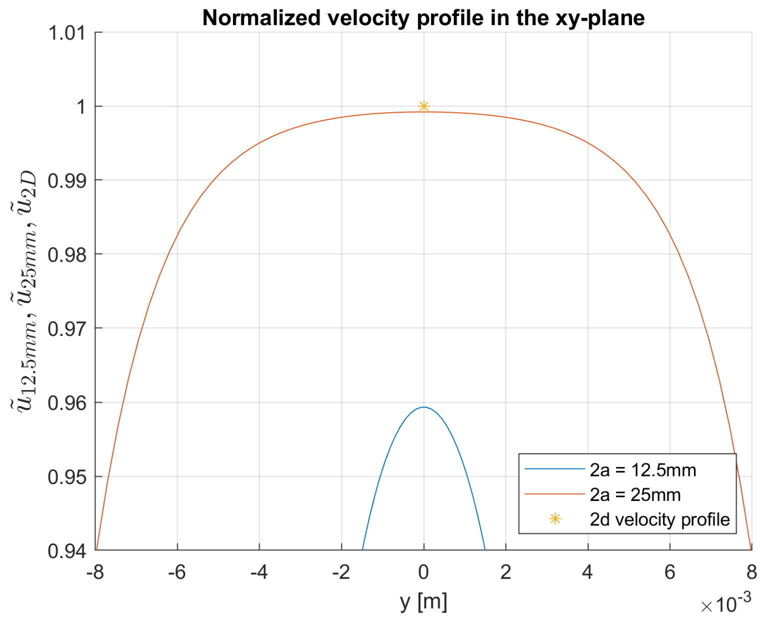

Figure 3.4: The normalized velocity profile for $2a = 12.5mm$ and $2a = 25mm$. The width is not non-dimensionalized to emphasise the impact the influence of the width of the channel to the velocity profile.

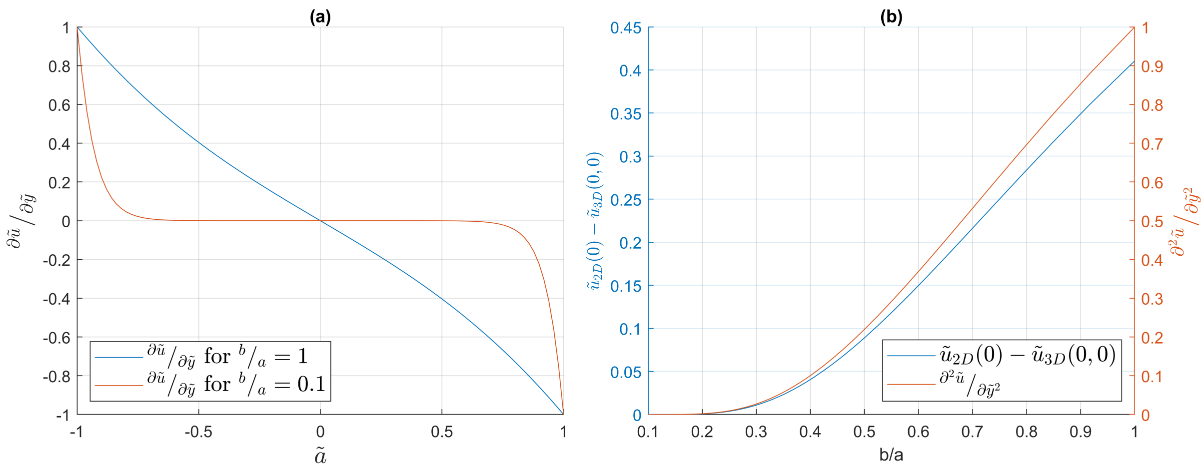

Figure 3.5: (a) First derivative of 3D velocity profile (eq. 3.5) with respect to y at $z = 0$. (b) Second derivative of 3D velocity profile (eq. 3.6) at $y = 0$ and $z = 0$ for different ratios of b/a. Also, the difference of the normalized 2D profile and 3D profile at $y = 0$ and $z = 0$ is plotted.

$u(y, 0) = 0.99u(0, 0)$ should not cause a problem.

The velocity profile of the fluid is location dependent, even though for the channel with $2a = 25mm$ there is some room in the y-direction without significant changes in the velocity profile (see equation 3.1). To get consistent results, the laser should be shot at the same location in the channel repeatedly. Shooting the laser at a constant y-coordinate also makes sure that the camera only needs to be focused once. The sample is rotated by $\Delta\theta$ so the laser can fire at a new location until a full ring is formed after which the sample is moved by Δx to shoot a new ring. This principle is shown in figure 3.7 (the figure is not to scale). $\Delta\theta$ and Δx will be chosen such that there are no other craters within a minimum radius of $300\mu m$. This will ensure that a con-vocal microscopy analysis of individual craters can be obtained. To distinguish the craters that are shot with different parameter sets (pulse frequency, pulse energy etc.), a

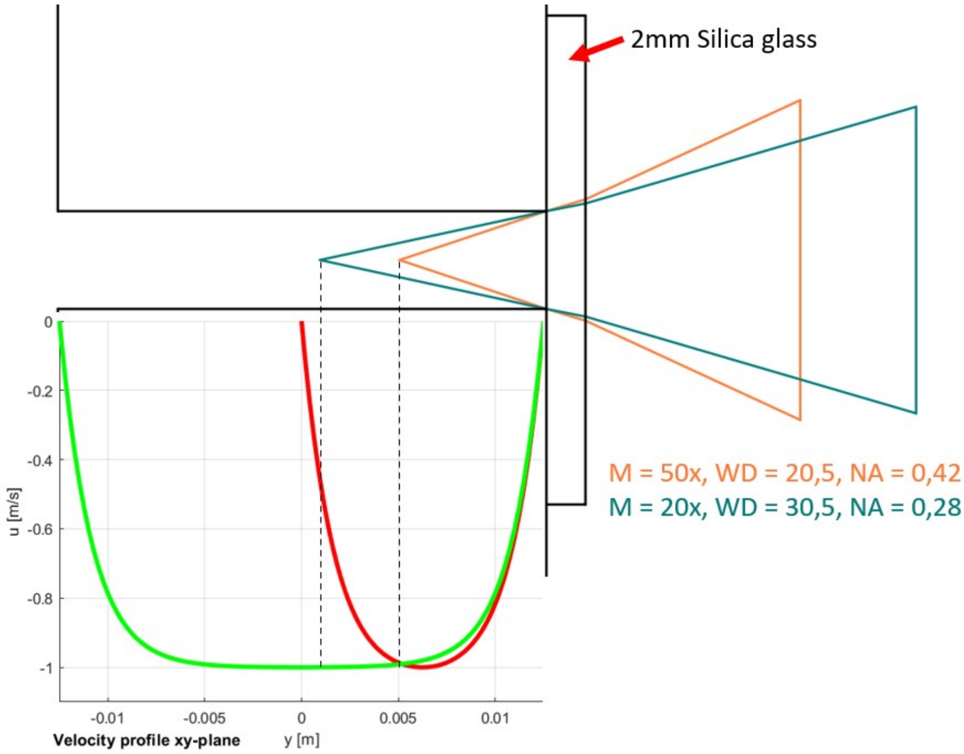

Figure 3.6: Cross-section of the channel with the optical path of two microscopes. The velocity profile in the xy-plane is placed across the cross-section of the channel.

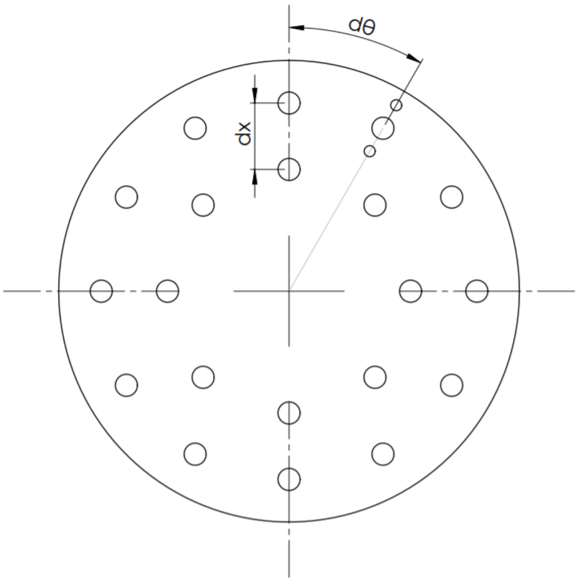

Figure 3.7: The crater pattern that will be shot on the rotating sample (not to scale). Each new test parameter set will be shot with two extra craters such that the craters shot with different parameters can be distinguished in a microscopy analysis.

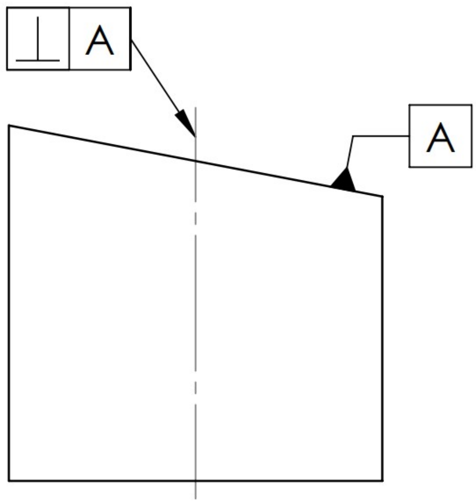

Figure 3.8: Indicating that the axis of rotation should be perpendicular to the face of the sample. In this exaggerated example the distance of the sample to the laser would change when the sample is rotated.

crater will be shot above and below the main crater.

3.4 Sample rotation and fabrication

The constraints on the distance between craters mean that the number of craters per sample is limited. Considering that a wide range of parameters must be tested and that replacing the samples between tests costs considerable time (water needs to be removed and replaced between a sample change), it is beneficial to shoot as many craters as possible on a single sample. Therefore, the channel width is chosen to be $25mm$ instead of $12.5mm$. Figure 3.9 shows a cross-section of the yz-plane at the x-location where the laser will be shot, and shows the mechanism that allows the sample to be adjusted in height and to be rotated between pulses. The 'height adjust' has a $M24x1$ thread and a ball bearing that constraints the sample movement in the z-direction, but allows the sample to be rotated by a motor via the 'driving axle'. The 'driving axle' has a $M4$ thread that threads into the sample and allows rotation in a single direction (turning in another direction would loosen the 'driving axle' from the sample). By turning the 'height adjust', the z-position can be adjusted such that the sample is flush with the channel.

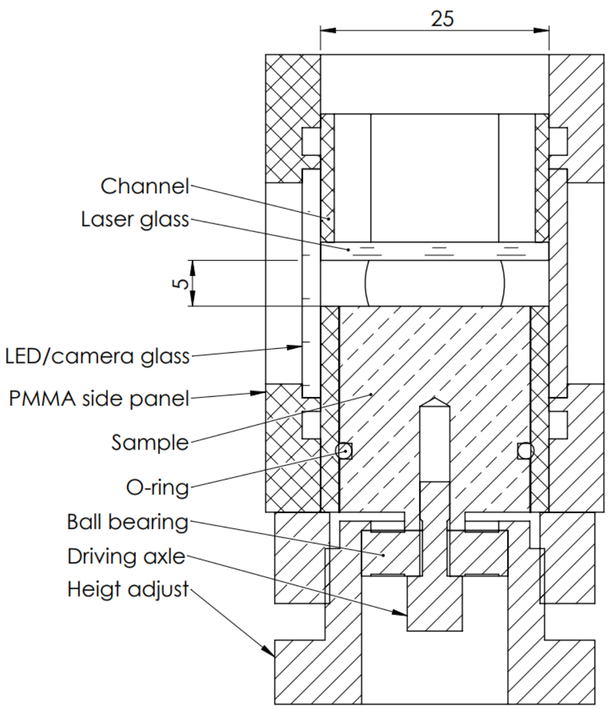

Figure 3.9: Components of the height adjust

The samples that are used in the laser tests in this report are made of stainless steel 304. They are machined from a single piece of bar stock. Samples of different materials can also be made by embedding them into epoxy by a Struers LaboPress-3. To do this, a sample piece is lowered in the machine and powdered epoxy is then dropped on the sample. The embedding machine then presses and heats this powder into a cylinder in which the sample is embedded. After embedding, the samples can be machined and fitted with an o-ring similar to the sample shown in figure 3.9. After machining the samples to size, they are polished on a Struers Tegramin-25 automated polishing machine with the steps shown in table 3.1. It is important that the face of the sample is perpendicular to the outside diameter throughout the process of making the sample. If the sample is not perpendicular, it cannot be mounted flush in the channel. Consequently it would introduce a height difference for the laser if the sample is rotated (see figure 3.8). The samples are stored in cleanroom boxes until use.

Step	Grid	Time	Pressure
1	320	1:30	30N/sample
2	500	2:00	30N/sample
3	1000	2:30	30N/sample
4	4000	2:30	20N/sample
5	MD-Chem	10:00	15N/sample

Table 3.1: Polishing steps for the samples using the specimen hold technique to process multiple sample at the same time.

3.5 Hydraulic entrance length

The hydraulic diameter D_h, which influences the entrance length, is determined by:

$$D_h = \frac{4ab}{a+b} \tag{3.7}$$

For $a = 12.5mm$ and $b = 2.5mm$ this results in a hydraulic diameter of $D_h = 8.3mm$. The hydraulic entrance length L_h, that is the length needed for the laminar flow to become fully developed ($u = 0.99u_{max}$ or $dp/dx = constant$), is determined by:

$$L_h = L^+_{h,D_h} Re D_h \tag{3.8}$$

L^+_{h,D_h} is a pre-determined dimensionless factor which value depends on the shape of the cross-section. For $\epsilon = b/a = 0.2$ the dimensionless entrance length is $L^+_{h,D_h} = 0.0326$ [44]. For a pipe with a circular cross-section, the transition zone of laminar to turbulent flow is from Reynolds 2300 to 4000. These values have not be found in literature for a rectangular cross-section. Therefore the same transition values will be assumed for the rectangular cross-section for now. The entrance length for turbulent flow is typically shorter than the entrance length for laminar flow [45]:

$$L_h \approx 1.6 Re^{1/4} D_h \quad for \quad Re \leq 10^7 \tag{3.9}$$

In the equation above the value for L^+_{h,D_h} is fixed at 1.6 independent of the cross-section. No cross-section dependent formula for turbulent flow could be found in the literature. The maximum length of the channel is mainly determined by the required entrance length for fully developed laminar flow. In the end, the chosen entrance length is a trade-off between the available room on the optical table, manufacturability and accommodating a fully developed flow. A Reynolds number of 2000, chosen for this design, gives a large range in Reynolds number for a fully developed laminar flow, while still allowing the channel to be mounted on the optical table. Combining $D_h = 8.3mm$, $L^+_{h,D_h} = 0.0326$ and $Re = 2000$ results in a hydraulic entrance length of $L_h = 543mm$.

3.6 Complete test setup

The entire channel is $695mm$ long. The channel is made from polyoxymethylene (POM, a plastic) as this material is cheap and easy to machine. POM is known for its dimensional stability and low friction coefficient which will help the sample rotation. The side panels are made from polymethylmethacrylate (PMMA), which is transparent so the inside of the channel can be viewed. In these side panels, grooves are cut for o-rings that seal off the sides of the channel. Circular infrared coated glasses ($\oslash 25mm$) from Edmund Optics are glued in the side panels for optical access by the LED and camera. Both ends of the channel are threaded with $G^1/_4$" gas thread for the hydraulic fittings.

The channel will be mounted to a $150mm$ square tube for extra support (see figure 3.10). Perpendicular to this tube, an aluminium profile is mounted to which a LED-pulser and a camera are mounted. The camera can be manipulated in the xyz direction relative to the channel with XR25C stages from Thorlabs. The LED-pulser can be manipulated in the xz-direction. As the light from the LED is collimated, a y-stage is not needed. In the tube a stepper motor, which will rotate the sample, is mounted. A line-light is mounted above the channel for PIV-measurements (next chapter). The line-light is removed for the laser tests as it would obstruct the laser. For a complete overview of how the system is used in the laser setup see figure 5.2 and 3.11.

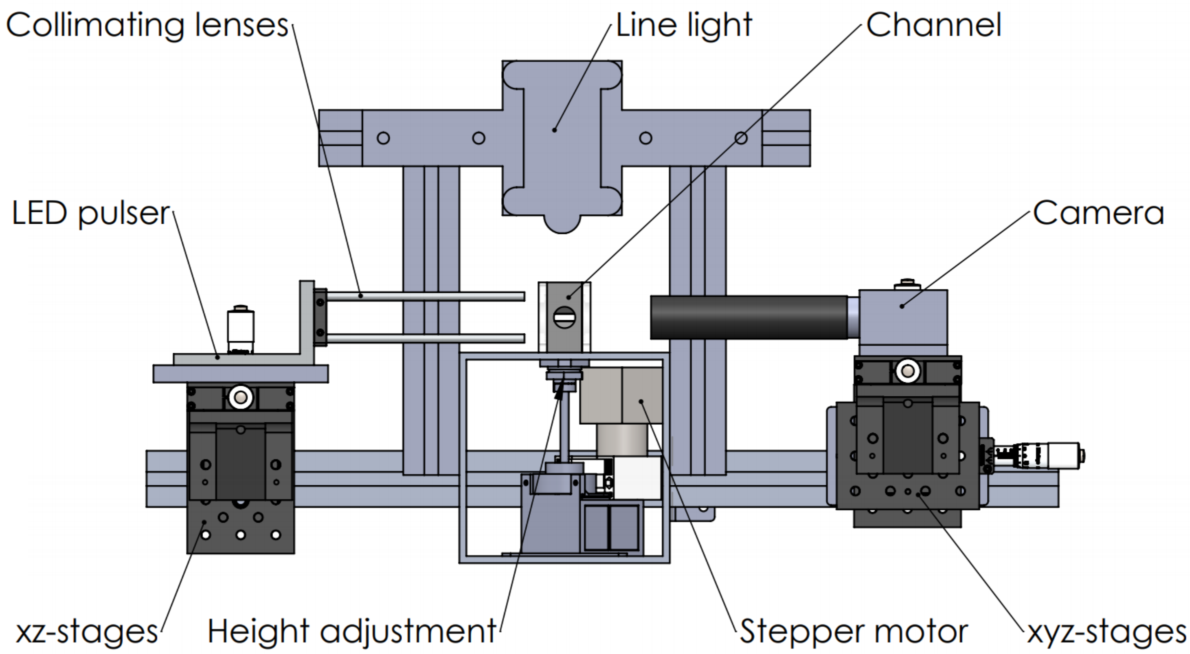

Figure 3.10: A view along the x-axis of the setup. The stepper motor and the LED-pulser were not used for the PIV-measurements and were initially removed. The line-light was later removed for the laser tests as it would otherwise obstruct the path of the laser (see also figure 5.2 for the laser setup).

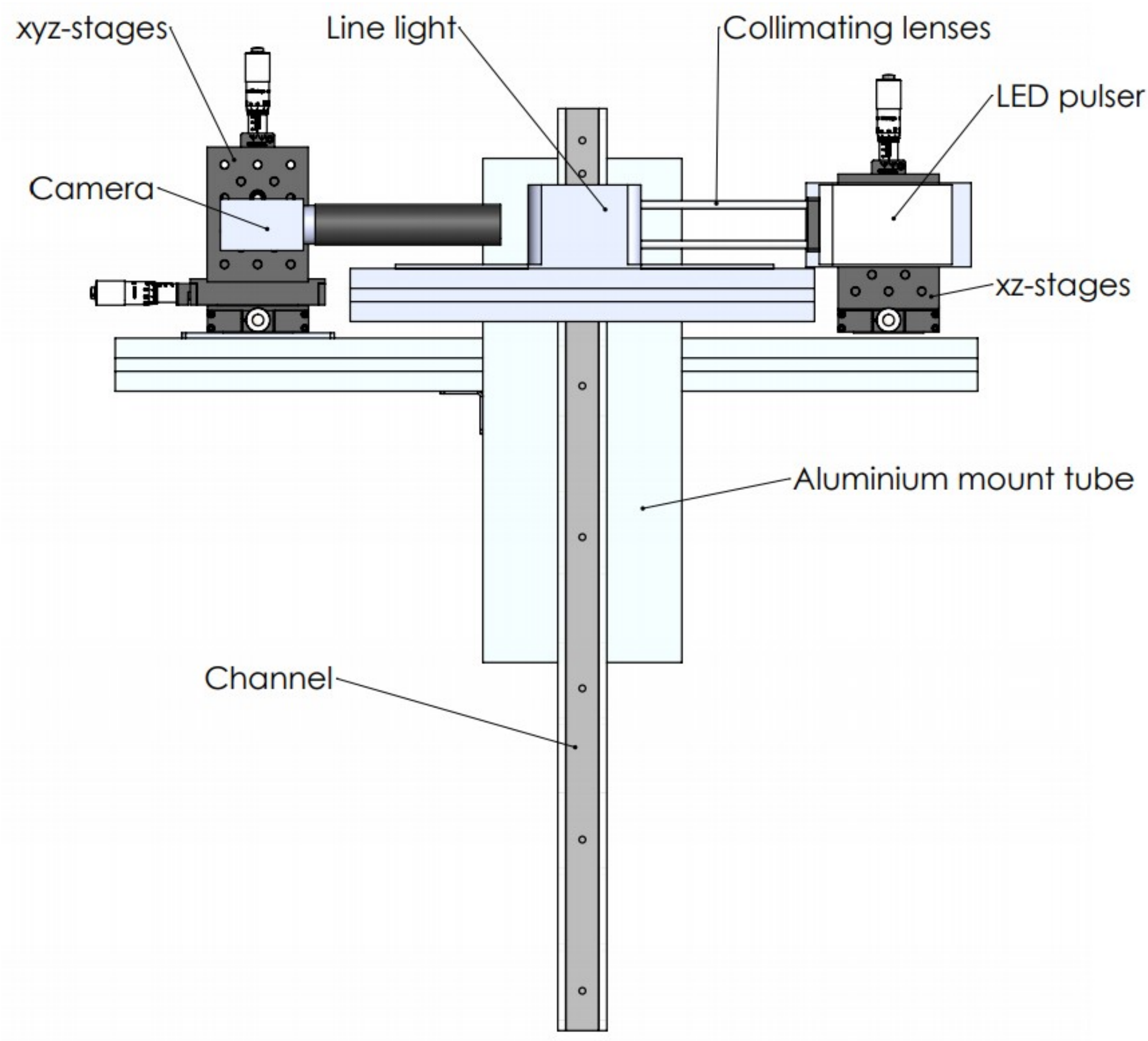

Figure 3.11: A top view of the setup

Chapter 4

PIV-measurements

The theoretical velocity profile, calculated with equation 3.1 will be verified with a particle image velocimetry (PIV) analysis. An overview of the system that is going to be used for these PIV tests is given in figure 4.1 and the components are listed in table 4.1. The components of the system will be discussed in their respective paragraphs below. Finally, the test procedure, data analysis and test results are treated.

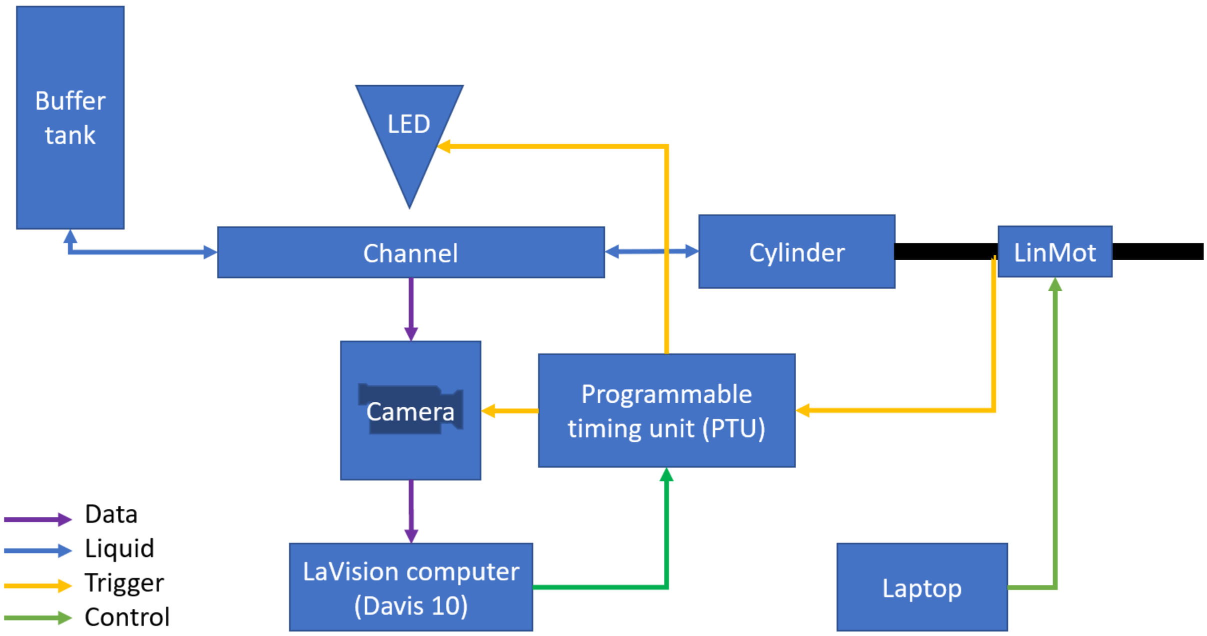

Figure 4.1: A system overview of the components that interact during the PIV-measurements.

4.1 Cylinder and linear motor

A linear motor acts on a cylinder to push the water, the liquid that is used in all tests, through the channel into a tube (buffer tank in figure 4.1) at the other end of the channel. On the return stroke of the cylinder, the water flows back from the buffer tank into the cylinder. The water will remain in the system and flows in both directions as indicated with the blue arrows in the system overview of figure 4.1. The PIV measurements will be done during the forward stroke of the cylinder, so the cylinder is connected to the 'long end' (the side of the channel with the hydraulic entrance length) of the channel.

A P01-37Sx120F motor with a $300mm$ rod from LinMot is used as linear motor. It is controlled using LinMot Talk 6.9 software. LinMot can control the stroke length, speed and acceleration of the linear

#	Component	Manufacturer
1	ISO 15552 IC50/125 pneumatic cylinder	PneuParts
2	Linear motor (LinMot) P01-37Sx120F	LinMot
3	300mm magnetic rod for linear motor	LinMot
4	SP-02 SinkPAD-II 7 Rebel LED	Luxeonstar
5	Focussing optic for 7 LED assembly	Luxeonstar
6	Line light assembly	Steven Wanrooij
7	LED pulser V3.1	Frans Segerink, Optical Science Group uTwente
8	SX9M camera	LaVision
9	Control computer for camera with DaVis 10	LaVision
10	Programmable Timing Unit (PTU)	LaVision
11	XR25c xyz-manipulation stages	Thorlabs

Table 4.1: Table with components that were used for the PIV-tests

motor via 'VA interpolator moves', which are trapezoidal velocity profiles. Trapezoidal velocity profile consist of an acceleration ramp, then a constant velocity followed by a deceleration ramp. The linear motor has a position feedback with a resolution of $0.005mm$, which was later used to create the velocity graph in figure 4.5. Initially, a custom hydraulic cylinder ($120mm$ stroke and a diameter of $50mm$) from Ares was used, but this cylinder leaked around the piston. The cylinder was replaced by a pneumatic cylinder (ISO15552 IC50/125 - $125mm$ stroke and diameter of $50mm$) from PneuParts to do all but 1 PIV measurement ($Reynolds = 13$). The cylinder and buffer tank were connected to the channel with tubes with an inner diameter of $8mm$.

The Reynolds number can be directly related to the cylinder speed v_{cil} by using equations 4.1 and 4.2. This conversion allows a PIV-measurement to be easily related to a certain Reynolds number.

$$u_{avg} = \frac{v_{cyl} A_{cyl}}{A_{channel}} = \frac{v_{cil} \pi r^2}{4ab} \tag{4.1}$$

$$Re = \frac{u_{avg} D_h \rho}{\mu} \tag{4.2}$$

The hydraulic diameter D_h is calculated in equation 3.7, the viscosity μ and the density ρ were taken to be $1.005 \cdot 10^{-3} kgm^{-1}s^{-1}$ and $1000 kg/m^3$ respectively. Together with the piston radius $r = 25mm$, the channel width $2a = 25mm$ and height $2b = 5mm$, the average velocity in channel becomes $u_{avg} = 15.7 v_{cil}$ and the Reynolds number becomes $Re = 1.30 \cdot 10^5 v_{cil}$. The maximum speed that the LinMot can create, was tested to be $0.09m/s$ or Reynolds 11721. The LinMot would give an error for higher speeds, as it requires too much force and thus too much current for the LinMot to drive the water through the channel.

4.2 Light source

A 7LED assembly from Luxeonstar (SP-02 SinkPAD-II 7 Rebel LED) was used to light up the PIV-particles. A focusing optic (also from Luxeonstar) was mounted on top of the LED to focus the light onto an optical fiber. The LED-assembly and optics were mounted in an aluminium enclosure that acts as a heat sink and as a way to fix the distance between the LED and the optical fibre (see figure 4.2 on the right). The optical fibers, grouped in a circle at LED-side of the fibers, transport the light to the channel. At the channel side, where the light exits the fibres, the fibres are grouped in a line. This 'line of light' is focused into a sheet with a width of $2mm$ and a depth of focus of $10mm$ by a semi-circle lens. The line-light was mounted $6mm$ above the channel and pointed through the laser glass, such that the focus of light is in the middle of the channel (see figure 4.2 on the left). The line-light could be moved in the y-direction, along the extrusion profile it is mounted to, in order to do PIV-measurements in another xz-plane.

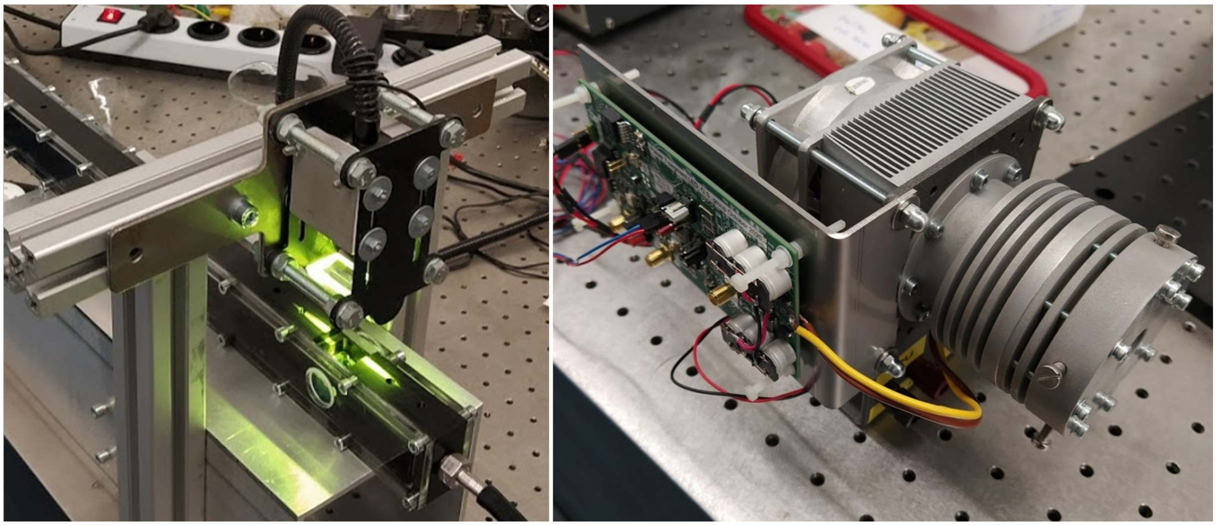

Figure 4.2: The line-light mounted above the channel on the left. The optical fibres run from the top to the LED-assembly in this figure on the right. The LED-pulser is mounted on the side of the LED-assembly.

Initially, the LED was powered by a LuxuenStar 2.1A BuckBlock driver for continuous lighting. Some test images with a PixelFly camera were shot with the available particles: Silica particles with diameter $0-20\mu m$ from Sigmund Lidner and silica particles with a diameter $40-70\mu m$ from Mühlmeier. Figure 4.3 shows the lighting condition with the smallest possible shutter time, which still allows particles to be seen. These images were shot with the continuous driver at a current of $1.8A$, driving the LED over its specified limit (this was possible without breaking the LEDs because of the heat sink and short duty cycle). Even though the LED was driven over its limit, the shutter speed should be lower still for higher flow speeds (to prevent motion blur, see the next paragraph 4.3), even for the bigger particles that light up more.

LEDs can be operated above their specified current to produce more light if the duty cycle is short [46]. Short being short enough to prevent thermal damage of the LED. Frans Segerink from the Optical Science group of the UT created a LED-pulser that can drive the 7LED-assembly with a maximum pulse of $17\mu s$ at $25A$. The LED was tested for an hour at a pulse frequency of $20Hz$ without illumination deterioration. The pulsed optical power at $25A$ is observed to be around 5 times higher than with a continuous operating current of $2A$. The optical power does not scale linearly with the current as the efficacy of the LED drops to around 35% at $25A$. The lighting conditions of the new LED-pulser were compared with the continuous driver. Unfortunately, the amount of light from the LED-pulser was still not enough to light op the $20\mu m$ diameter particles at lower shutter speeds. This is unfortunate, as the smaller particles remain in suspension longer than the bigger particles, which have the tendency to either float or sink faster than the small particles. The LED-pulser does create enough light to light up the bigger particles with a pulse duration of $17\mu s$.

4.3 Camera

A PixelFly camera by PCO was used for some initial tests to see what particles should be selected and if the lighting was enough to do a PIV-measurement (see previous paragraph). However, the PixelFly cannot shoot pictures fast enough at high flow speeds. The same particles should be photographed twice for a measurement, so the camera has to be able to take two pictures in rapid succession. The

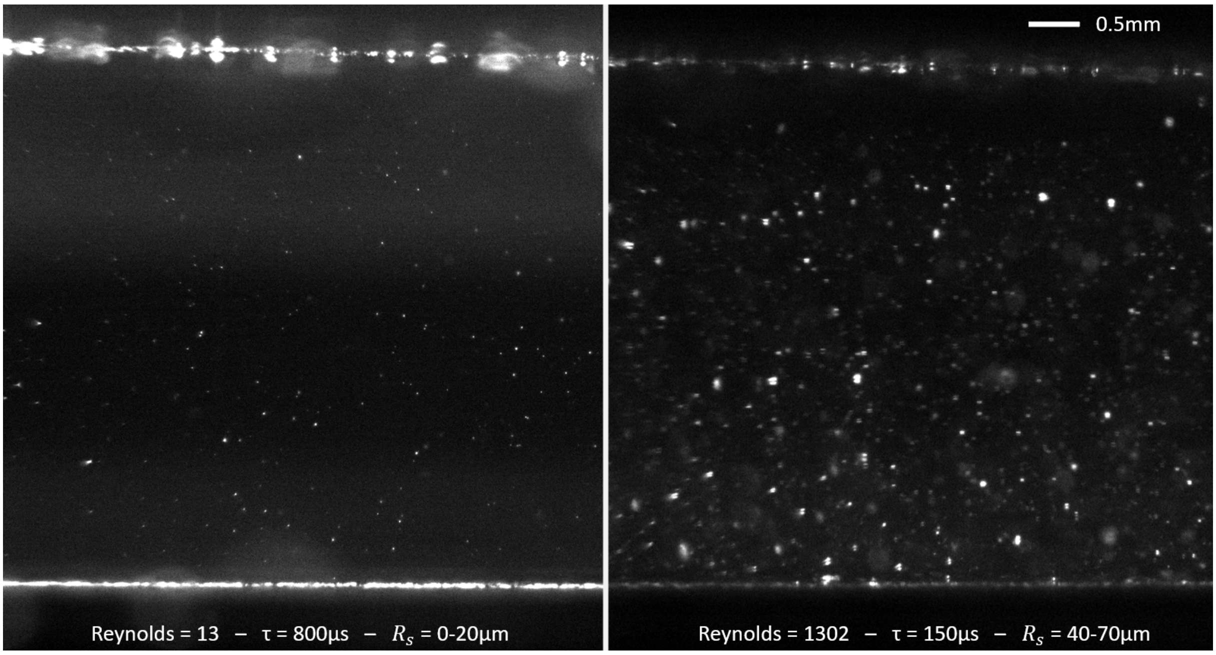

Figure 4.3: A comparison in lighting conditions between the different particles sizes (R_s) with continuous lighting.

required imaging frequency f is a function of the maximum particle velocity u_{max}, the camera magnification M, the pixel size of the camera r_p and the particle displacement in pixels between frames s_p. The maximum particle velocity can be estimated with the 3D velocity profile of the flow (equation 3.1). The particle displacement between frames s_p is taken to be 50 pixels (this choice is literature based [47]). Noting that $u_{max} = 1.75u_{avg}$ for the dimension of the cross-section of the channel ($2a = 0.025mm$ and $2b = 0.005mm$), the required camera frame frequency becomes:

$$f = \frac{u_{max}M}{r_p s_p} = \frac{1.75\mu ReM}{D_h r_p s_p \rho} \tag{4.3}$$

The temporal resolution τ determines how fast the camera or light source should be to avoid motion blur. Motion blur occurs when an object moves more than one pixel during camera exposure. Equation 4.4 was used to calculate the required temporal resolution to prevent motion blur for the PIV-measurements. Equation 4.3 and 4.4 are plotted in figure 4.4 for the listed camera's in table 4.2. The camera's in table 4.2 are the camera's that were available at the time of the PIV-measurements. The camera and pulse width of the LED-pulser were selected based on figure 4.4. It shows that for higher flow speeds τ goes to $10\mu s$ for all cameras. The pulse duration of the LED-pulser is set to $17\mu s$ even though τ should be 10, because every bit of light is needed to get enough contrast in the measurements. Also, some motion blur forms no problems for PIV analysis. This based on some tests with the software using pictures like in figure 4.3 on the right. The conditions in which the picture in figure 4.3 on the right is taken, is plotted in figure 4.4 with a asterisks. The motion blur is estimated to be 6 pixels.

$$\tau = \frac{r_p}{Mu_{max}} = \frac{r_p D_h \rho}{1.75\mu MRe} \tag{4.4}$$

The PixelFly is unsuited for the PIV measurements in its current configuration, as the frame rate is too low. The PixelFly has the option to have a shorter interframe time, but this option is not installed on the camera at hand. Some cameras (PixelFly and Imager SX9M for example) are able to take two pictures in short succession at a low frame rate. This is especially useful for a PIV measurement. Considering the Phantom v711 and the Imager SX9M: Both cameras are fast enough, but the frame size

Cameras	PixelFly	SX9M	SX9M binned	Phantom v711
Pixelsize (r_p)$[\mu m]$	6.45	3.69	7.38	20
Resolution	1392x1040	3360x2712	1680x1356	1200x800
Magnification	1.15	1.15	1.15	3.2
min. interframe time, max fps	0.13s/13.5 fps	150ns/14.92fps	500ns/14.92fps	130ns/7530fps
Quantum efficiency [%]	62	45	45	-

Table 4.2: A table with specification of the cameras that were available for the PIV-measurement

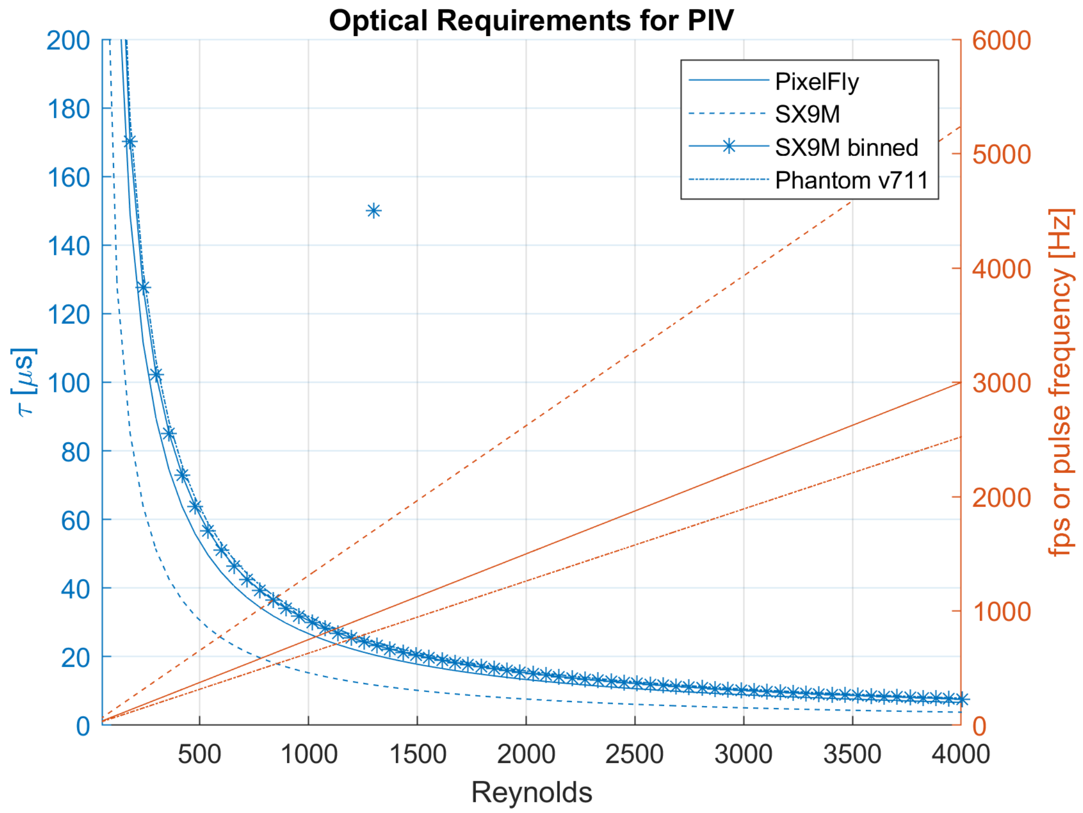

Figure 4.4: Temporal optical requirements for PIV for several cameras. The single asterisk is the position of the picture on the right in figure 4.3 above.

of the 9M corresponds better with the height of the channel. Therefore less magnification is needed and the lens was readily available since it could be remounted from the PixelFly. Considering all these factors, the SX9M with horizontal and vertical binning was chosen for the PIV-measurements. Binning increases the sensitivity to light and reduces the signal to noise ratio of the sensor, by combining 4 pixels (2 horizontal and 2 vertical) into a single pixel.

4.4 Software

The SX9M camera is controlled by a dedicated computer with a DaVis10 software package from LaVision. The computer programs the Programmable Timing Unit (PTU) that handles the triggering of the LED and camera (see figure 4.1). A limit switch placed on the rod of the LinMot triggers the system to start recording, triggering the LED to flash and the camera to take pictures in sync with each other. The pulse width of the LED is controlled via the DaVis software and is set to $17\mu s$. The camera is set to have a shutter time of $40\mu s$ on the first frame, a delay time between frames of $1000\mu s$ for lower flowspeeds ($Reynolds < 1300$) and $500\mu s$ for higher flow speeds ($Reynolds > 1300$). Ideally, the time between frames should scale with the Reynolds number (equation 4.3), but to prevent errors in the subsequent PIV-analysis and to speed-up the measurements, these two fixed time-intervals are chosen. This is done because the camera is only available for a limited time. The shutter speed of the second frame is determined by the readout time of the first frame, which takes up several hundred microseconds. The PIV-measurements are done in the dark, to make sure that the lighting condition are the same for both frames. In that way the only light on the camera comes from the line-light. The number of frames for each test are adjusted so the camera takes pictures of the whole event, which is from the point of triggering at the beginning of the stroke to the end of the stroke. The number of frames is dependent on the speed of the LinMot since the frame rate of the camera is fixed at $14.92 fps$.

The DaVis software package contains PIV-analysis software. However this software is not used for the analysis as the computer and camera are only available for a limited amount of time. Instead, PIV-lab created by William Thielicke for Matlab is used to analyze photos. The images are loaded as pairs and pre-processed, to increase the particle's visibility and contrast. A fast Fourier transformation with a 3 pass interrogation window, starting at 150 pixels down to 32 pixels is used to perform the PIV-analysis. These settings are based on theory, the DaVis FlowMaster manual and largely on trial and error to obtain satisfactory results [47]. The data is calibrated by selecting the top and bottom of the channel (these were visible as reflection on the image) giving a distance in pixels and correlating this distance by the real channel height ($5mm$). The inter-frame time is known allowing the software to calculate a speed based on the displacement in pixels between the two frames. The velocity component u (x-direction) is extracted from the data from a line in z-direction in the centre of the frame, the option 'extract data from poly-line' in PIV-lab. The PIV-lab software has an option to extract the complete vector field (not just a single line), but this function was not working at the time.

4.5 Test procedure

The channel and cylinder are filled with demineralized water and are vented by moving the cylinder so any air can escape from the open end of the buffer tank. The PIV-particles are added with a pipette as a suspension of particles and water with $1mL$ per addition. The particles have a tendency to drop out of suspension and more is added during the testing to compensate for that. For the flows with a Reynolds number up to 3907 a two stage velocity profile is loaded in the LinMot (see the demand cylinder curve in figure 4.5). An initial 'push' of $0.06m/s$ of $40mm$ is used to get the particles into suspension at the lower speeds. The velocity of the remainder of the stroke is set to the specific test condition. The LinMot is set with a single velocity for Reynolds bigger than 3907. For each test the cylinder is moved to the top of its stroke. Then the camera and LED system is set ready to be triggered. The LinMot is set into motion and the camera starts taking pictures until the predetermined amount of pictures is reached. Then the LinMot is returned to the top of its stroke, a new velocity is set and the cycle repeats. Each velocity is tested three times with a few exceptions: the velocity profile in different xy-planes is tested only once and the test at Reynolds = 13 is also performed only once. The pictures are exported from the DaVis computer and loaded into PIV-lab and analyzed.

4.6 Data analysis

All the velocity data $u(z)$ from one image sequence are exported per frame as a $.csv$ file. These data can be assembled for a complete data set $u(z,t)$ of a single stroke at a certain velocity of the LinMot. The u-velocity from $z = -1$ to $z = 1$ was averaged and plotted in figure 4.5. The u-velocity was averaged around $z = 0$ for several reasons. First, averaging the velocity means that the velocity can now be graphed in a 2D plot ($u(z,t) \to u(t)$) which makes visualisation easier. Secondly, the velocity data at the top and bottom of the channel is inaccurate due to poor seeding of the particles and would lead to a large error on the average velocity. The big particles sink more easily to the bottom and are then dragged along by the flow. The PIV-analyzer has difficulties analyzing these poorly seeded parts of the channel resulting in significant swings in the velocity profile. Finally, this average velocity of the centre more clearly shows when the flow is fully developed, which is explained in depth in the next paragraph.

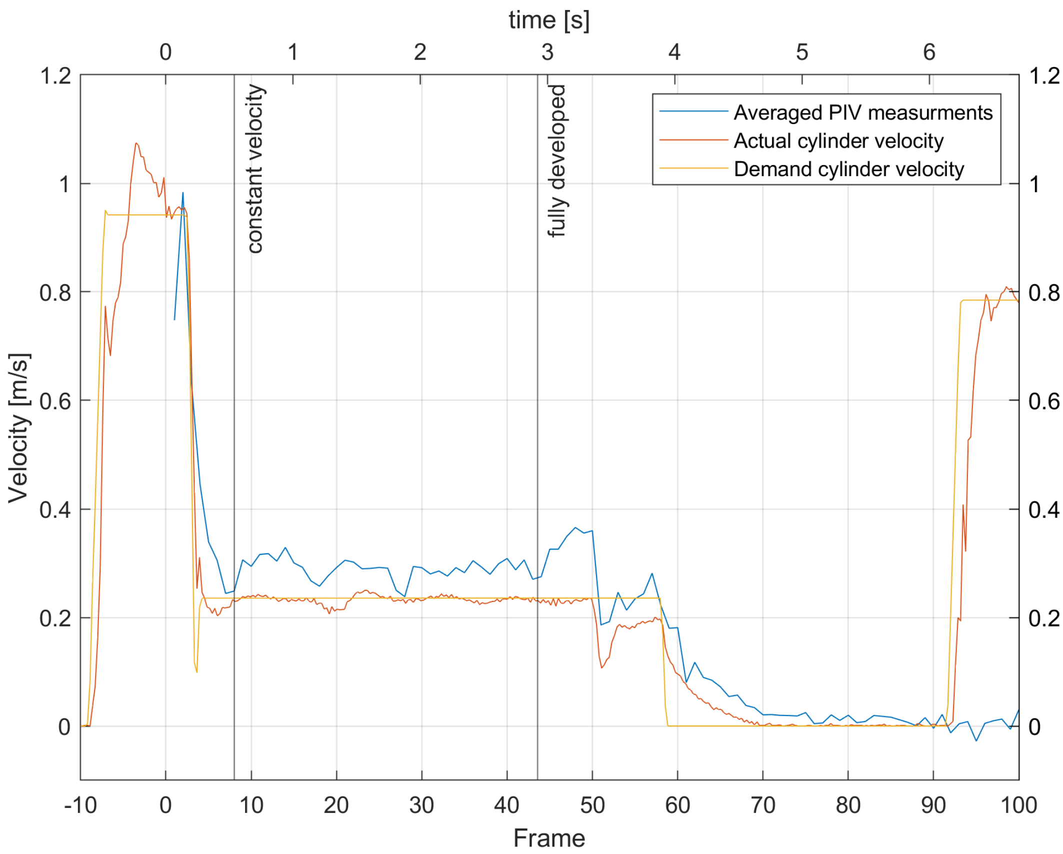

Figure 4.5: Transient velocity data $u(t)$ of a PIV-measurement at Reynolds = 1953. The blue line represent the average u-velocity of the data from the centre 2mm. The actual cylinder velocity was constructed by differentiating the positional data from LinMot talk and scaling it by equation 4.1 to get u_{avg}. The demand velocity represent the trapezoidal velocity profile the LinMot was set to create. The initial peak of the cylinder velocity is used to get PIV-particles in suspension. The cylinder velocity is taken at a different moment than the PIV-measurement explaining the discrepancy between the velocities at the end of the stroke.

A flow does not instantaneous develop. For some scenarios the time it takes for a flow to fully develop can be calculated [48]. For the situation analysed in this these, a constant flow rate, no such formulas could be found. When looking at the graph in figure 4.5, there is a clear peak in the velocity, starting at frame 43 and ending at frame 50, which is the end of the stroke. The velocity profiles of these frames are averaged and plotted in figure 4.6 on the right. The velocity profiles from the moment that the cylinder is at constant speed after the initial push (frame 6) to frame 43 is plotted on the left. Clearly, the manual selected frames (frame 43 to frame 50) match closely to the theoretical velocity profile. The velocity profile on the right shows a 'flat' centre, which indicates that the flow has not had enough time to develop.

To prevent bias in selecting the frames that show fully developed flow, a formula is created to select the right frames (equation 4.5). First, the moment that the cylinder is at constant speed after the push

$t_{constant}$ is selected (also indicated in figure 4.5). Then, the hydraulic entrance length L_h is divided by the average flow velocity u_{avg} and multiplied by the camera's frequency to get the number of frames after $t_{constant}$. This yields the frame number for which the flow is deemed to be fully developed t_{FD}. The formula implies that the time it takes for a flow to fully develop is the time it takes for the flow to travel the entrance length L_h. To get a sense of accuracy of this formula, figure 4.7 is created. It shows the difference in frames when manually selecting the 'peak' in figure 4.5 and using equation 4.5. Figure 4.7 only contains the Reynolds range where the velocity peak could manually be selected.

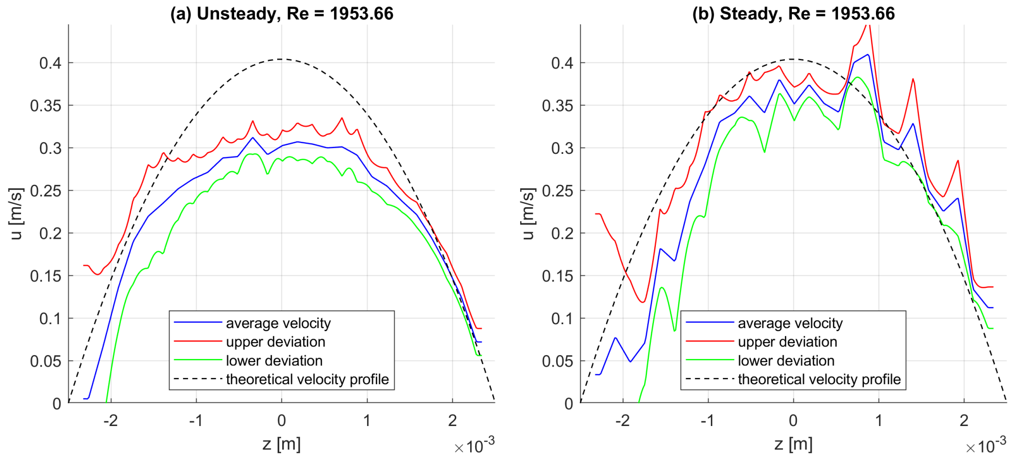

Figure 4.6: Velocity profiles along the line y = 0. (a) $u(z)$ derived from frames 6 to 43 from figure 4.5. The blue line is the average velocity. The red and green lines are the standard deviation from the average. (b) $u(z)$ derived from the velocities from frame 43 to 50.

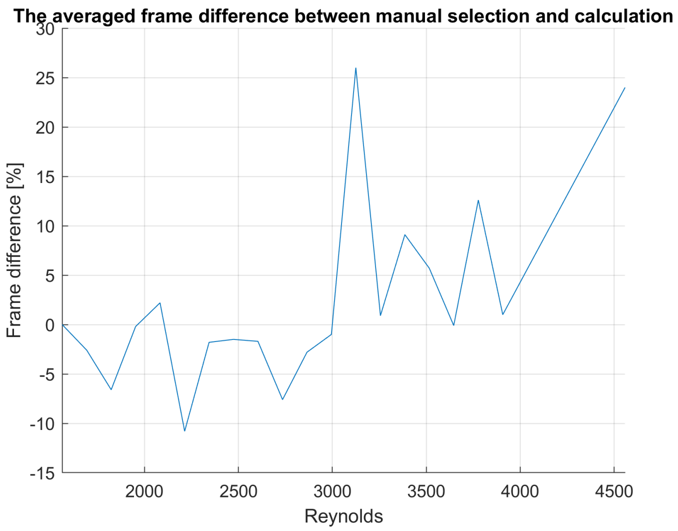

Figure 4.7: Difference between manual selection the right frame for the start of the fully developed flow versus the frame that is calculated with equation 4.5. The range in Reynolds in this graph is limited to where manual selection of the frames was possible.

$$t_{FD} = \frac{L_h}{u_{avg}} f_{camera} + t_{constant} = \frac{0.541}{u_{avg}} 14.92 + t_{constant} \tag{4.5}$$

It might be argued that the big seeding particles are bad tracers and the peak in the graph might come from the push in the beginning because the particles still have that initial speed from the push.

However, the particles seem to follow the cylinder velocity quite well. Especially looking at the similarity in velocity of the cylinder and particles at the end of the stroke (starting at frame 50). This makes it unlikely that effects of the push would carry on for that many frames. The Reynolds range in figure 4.7 corresponds quite well with the Reynolds range where the push was used ($13 < Reynolds \leq 3907$) and could well be the reason for that peak. At this point it was not possible to investigate the real cause for the peak and equation 4.5 will be used as best method for selecting the right frames.

4.7 PIV results

The PIV-measurements result in a substantial data set with velocities in the fully developed time range $u(y, z, t, Re, n_{tests})$. To reduce the size of the data set, the velocities for all the frames of the different tests (n_{tests}) at the same Reynolds number are added together and averaged: $u(y, z, t, Re, n_{tests}) \rightarrow u(y, z, Re)$. The velocities are normalized by dividing the velocity $u(y, z, Re)$ with the theoretical velocity $u_{3D}(y, z, Re)$. The theoretical profile is calculated by equation 3.1. To determine the pressure gradient, equation 4.6 is used (rewritten from equation 3.2) where the flow rate Q can be calculated with equation 4.7.

$$-\frac{dp}{dx} = Q/\left(\frac{4ba^3}{3\mu}\left[1 - \frac{192a}{\pi^5 b}\sum_{i=1,3,5,...}^{\infty}\frac{tanh(i\pi b/2a)}{i^5}\right]\right) \tag{4.6}$$

$$Q = A_{cil}v_{cil} = \frac{A_{cil}Re}{1.30 \cdot 10^5} \tag{4.7}$$

The measured data is normalized by dividing it by the maximum value of the theoretical profile:

$$\tilde{u}(y, z, Re) = \frac{u(y, z, Re)}{u_{3D}(0, 0, Re)} \tag{4.8}$$

The theoretical velocity profile is also normalized:

$$\tilde{u}_{3D}(y, z, Re) = \frac{u_{3D}(y, z, Re)}{u_{3D}(0, 0, Re)} \tag{4.9}$$

Now the graphs in figure 4.8 (a) and 4.8 (b) can be created, allowing easy comparison between different flow speeds. From figure 4.8 (b) it becomes clear that the velocity profile cannot fully develop anymore at higher flow speeds. The form of the velocity profile becomes flatter and doesn't follow the parabolic theoretical profile anymore. To get an overview of how the measured velocity profiles deviate from the theoretical profile, the difference between their peaks is calculated with equation 4.10 and plotted in figure 4.9. The maximum of the measured data at the centre of the channel ($y = 0$) in the range $-1 < z < 1$ is used $\tilde{u}_{max}(Re) = max(\tilde{u}(0, z, Re))$, as the maximum velocity is not always positioned at $z = 0$ and the velocity at the edges can be higher than in the centre (see figure 4.8 (a) as example).

$$\Delta\tilde{u}(Re) = \tilde{u}_{3D}(0, 0, Re) - \tilde{u}_{max}(Re) \tag{4.10}$$

The gray band in figure 4.9 signifies the standard deviation of the measurements. This deviation is bigger for lower Reynolds numbers, as the seeding particles dropped from suspension making it hard for PIV-lab to do accurate calculations on the velocity profile. Not being able to do measurements due to poor seeding conditions at low flow velocities is also the reason why there are no measurements for $Reynolds < 520$ for one exception at $Reynolds = 13$. The measurement at $Reynolds = 13$ is done with the PixelFly camera with the small particles ($20\mu m$ diameter) with continuous lighting. A higher value of $\Delta\tilde{u}$ indicates that the flow deviates from the theoretical fully developed profile, so as expected, the value of $\Delta\tilde{u}$ starts increasing after a Reynolds number of 2000. There are two outliers at Reynolds 2214 and 3516, which might be explained by errors in the data processing, confusing cylinder speeds measuring

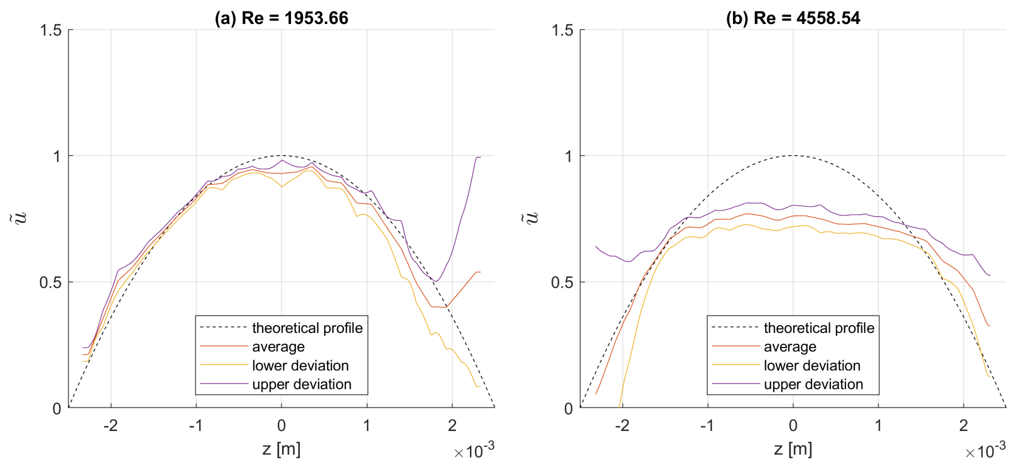

Figure 4.8: (a) the assembled and normalized data for all the measurements at $Re = 1954$. (b) the assembled and normalized data for all the measurements at $Re = 4559$.

lower velocities than expected. The outliers at the higher Reynolds range ($Re > 10^4$) can be explained by the lack of pictures at these high speeds, because the camera is too slow (a stroke of the LinMot is finished in less than a second).

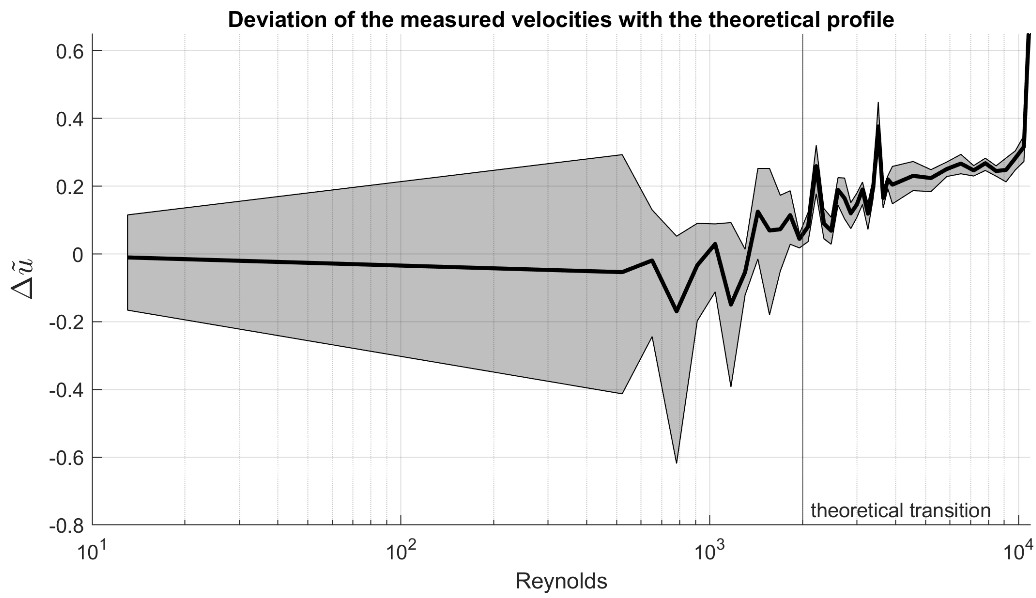

Figure 4.9: $\Delta\tilde{u}(Re)$ plotted on a logarithmic scale of Reynolds. The grey band around $\Delta\tilde{u}(Re)$ (black line) is the standard deviation of the measurements. The graph contains all the measurements done at $y = 0$.

Measured velocity profiles $\tilde{u}(y, 0, Re)$ in the range $0 \le y \le 9mm$ are plotted in figure 4.10 to figure 4.14. These are measurements only done once for a certain speed, whereas the data in figure 4.9 consists of three measurements for each cylinder speed. The y-range was limited to $9mm$ because the line-light was at the edge of the laser glass and unable to illuminate the PIV-particle for a bigger y. Figures 4.10 to 4.14 show that the flow approximates a 2D flow in the range $0 \le y \le 9mm$, just like the theoretical profile.

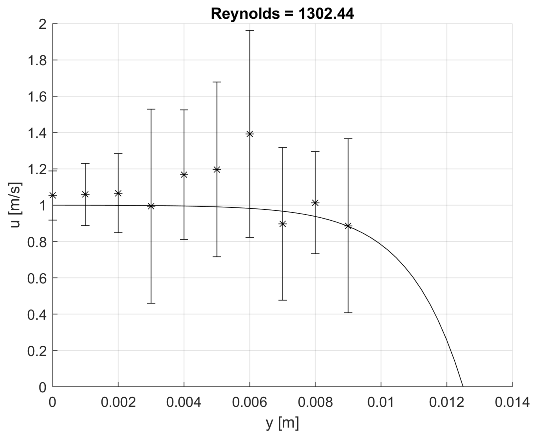

Figure 4.10: Velocity measurement in the xy-plane for $Re = 1302$.

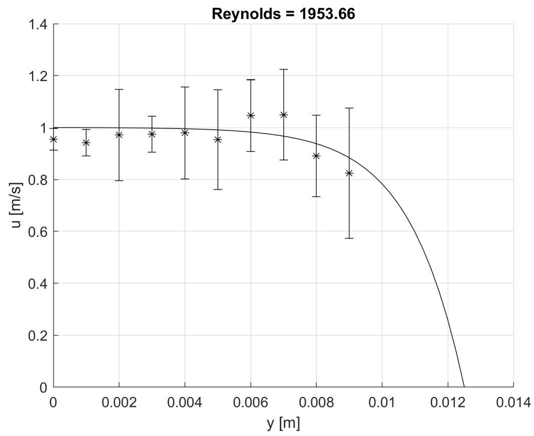

Figure 4.11: Velocity measurement in the xy-plane for $Re = 1953$.

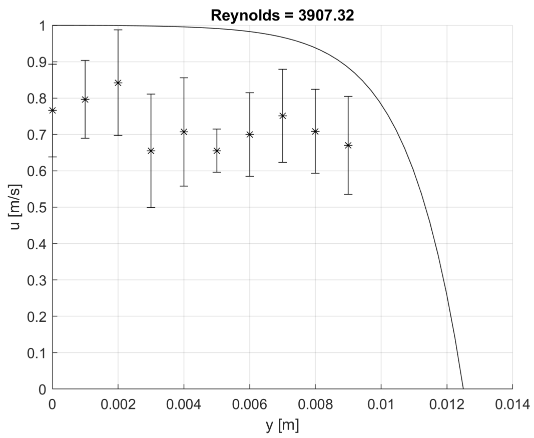

Figure 4.12: Velocity measurement in the xy-plane for $Re = 3907$.

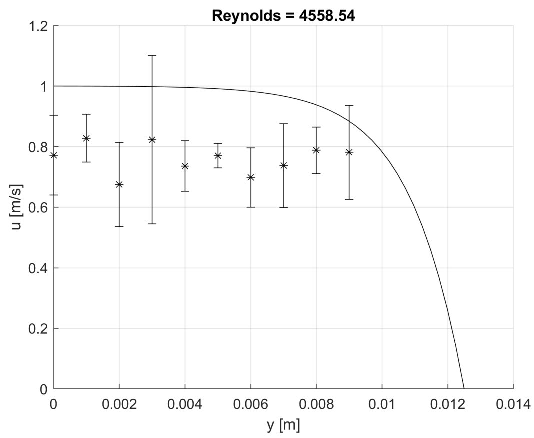

Figure 4.13: Velocity measurement in the xy-plane for $Re = 4559$.

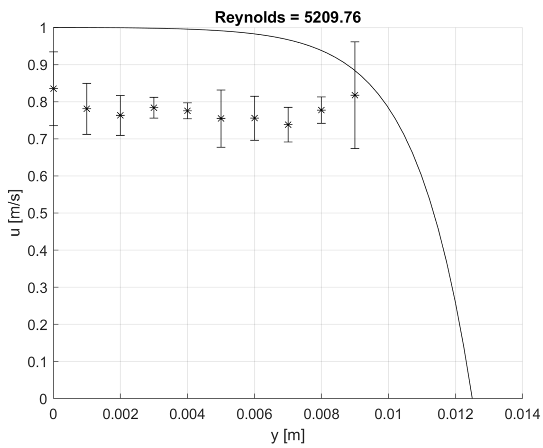

Figure 4.14: Velocity measurement in the xy-plane for $Re = 5210$.

Chapter 5

Laser tests

For the laser tests some additional components, aside from those used in the PIV analysis, are needed. The interaction schematic of these components are shown in figure 5.1 and listed in table 5.1. A 3D representation of the complete setup is shown in figure 5.2. The function of the additional components will be explained in their respective paragraphs below. Afterwards the setup procedure for aligning the laser and determining the focus is explained. Finally, the test procedure and test results will be discussed.

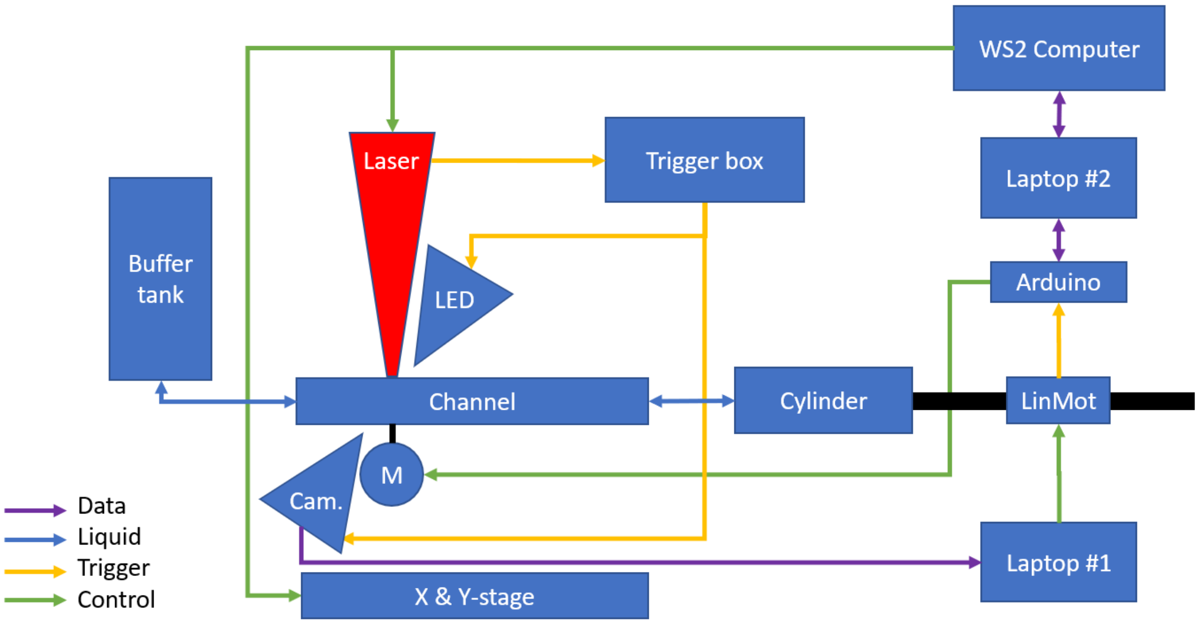

Figure 5.1: The schematic overview of the laser setup with its major components.

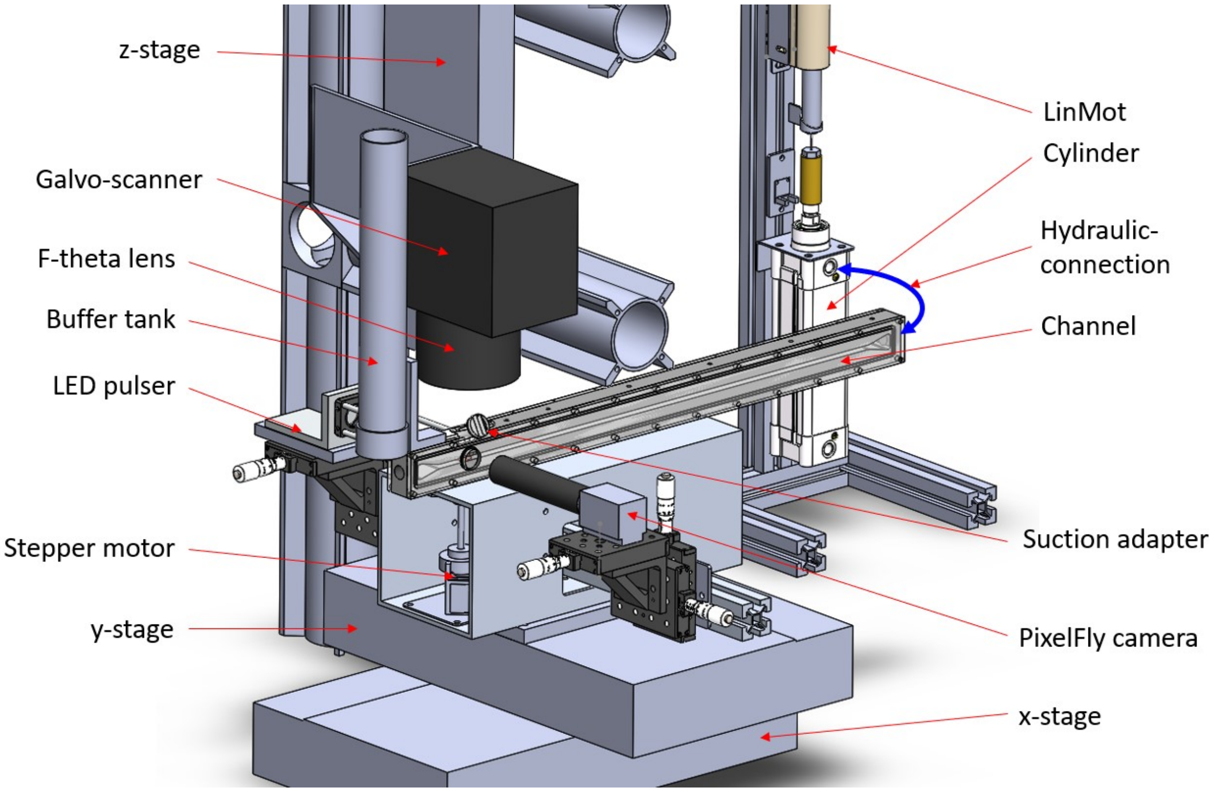

Figure 5.2: A 3D representation of the laser setup. The gantry to which the z-stage is mounted is partially cut-away for a better view.

#	Component	Manufacturer
1	ISO 15552 IC50/125 pneumatic cylinder	PneuParts
2	Linear motor (LinMot) P01-37Sx120F	LinMot
3	300mm magnetic rod for linear motor	LinMot
4	V3.1 LED pulser + LED	Frans Segerink, Optical Science Group uTwente
5	Collimating lenses (opzoeken)	Mitutoyo
6	PixelFly camera	PCO
7	BNC 577 trigger box	Berkeley Nucleonics Corp
8	NEMA17-05GM bi-polar stepper motor	JOY-IT
9	Po-Step25-32 driver	JOY-IT
10	Arduino UNO	Geekcreit
11	ALS20020 x&y stages	Aerotech
12	ALS2000 z-stage	Aerotech
13	A3200 drivers	Aerotech
14	intelliSCAN 14 with F-theta ronar lens $f = 80mm$	Scanlab
15	XR25C xyz-manipulation stages	Thorlabs
16	G4 Pulsed Fibre Laser	SPI Lasers
17	BC106-VIS beam profiler	Thorlabs
18	FieldMaxII power meter with 10W probe	Coherent
19	DET10A/M photodiode	Thorlabs

Table 5.1: The list of components that were used for the laser tests

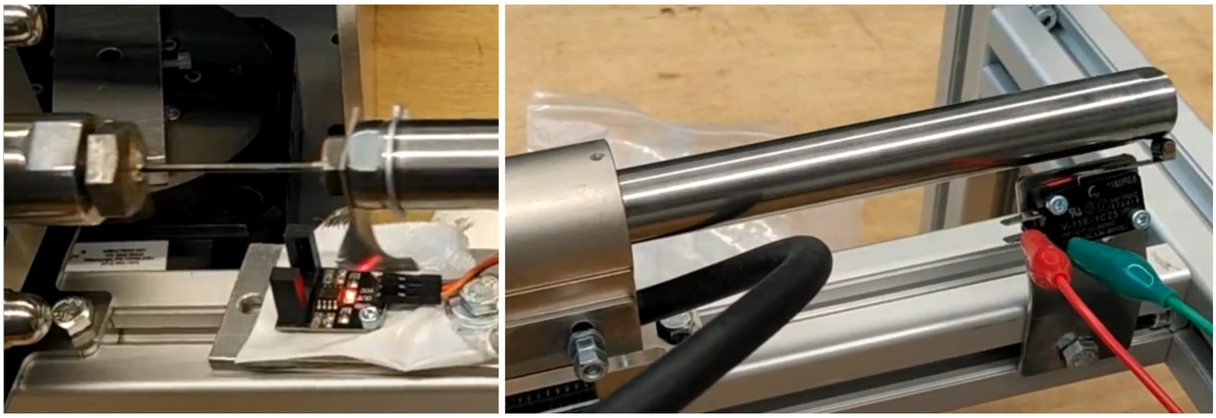

Figure 5.3: The opto-interrupt (left) and the limit switch (right) that are used to determine the position of the cylinder.

5.1 Arduino

The workstation 2 computer runs a Python script that controls when the laser should be fired and where the xy-stage (ALS20020 stages driven by A3200 Aerotech drivers), to which the channel is mounted, should move. The laser should be shot when the flow is fully developed, which depends on the position of the cylinder. After a certain stroke length, the flow has become fully developed (see previous chapter for more explanation). A mechanical switch is placed at the position in the stroke where the flow is fully developed (figure 5.3 right). An opto-interrupt is placed at the end of the stroke, so the laser computer will know when to stop firing the laser (figure 5.3 left). Here an opto-interrupt was used because there was no place for a switch, but their working principle is the same. They are wired according to the diagram in figure 5.4.

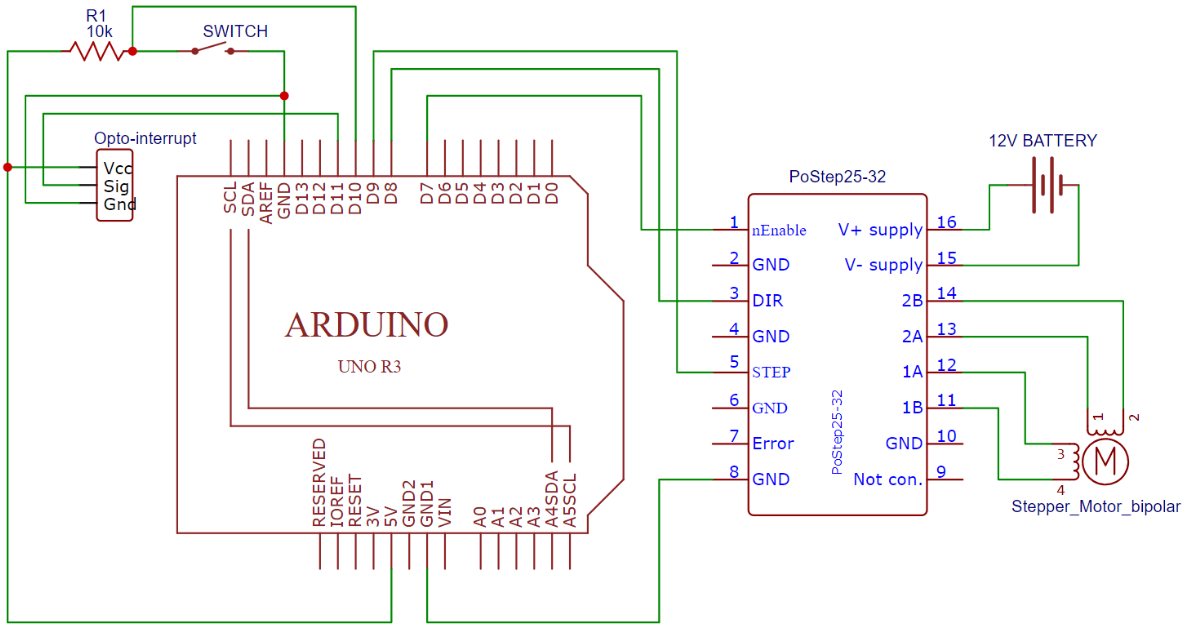

Figure 5.4: The Arduino diagram for the laser tests. The Arduino is connected to a laptop via the USB-interface

The Arduino (uno) should communicate the position of the LinMot to the laser computer, but the Arduino could not be directly coupled to the laser computer. If the Arduino was connected to anything that was powered by the power grid, the communication from Arduino produced random data. Examples of things that caused problems when connected are: the laser computer, a laptop with charger, a bench power supply for the stepper driver and even a camera that was powered by the grid and connected to a laptop which was connected to the Arduino. The cause of the problems seems to be the xy-stages When they were turned on the communication problems started. It remains unclear what the root cause is. Electromagnetic radiation or a ground loop are probable causes. As workaround for the problem, all the cables were wrapped in aluminium and the Arduino was placed in a metal container, acting as a Faraday cage, to keep the EM-radiation away. The Arduino is powered by a laptop which is not connected to the grid. The stepper motor is powered with a battery, effectively disconnecting all but the WS2 computer from the power grid.

The Arduino laptop runs a script with PySerial to communicate with the Arduino via Python. The laptop in turn communicates to the laser computer via an UTP-cable on LAN using Socket in Python. The UTP-cable does not transport power and has twisted wires to prevent problems with EM-radiation. The UTP-cable does not cause communication problems in the system. The Arduino also controls the stepper motor that is used to rotate the sample after a crater is shot. A two-way communication is needed between the laser computer and Arduino, since the laser computer does not only need to know when to fire the laser, but it also needs to let the Arduino know when to rotate the sample. A NEMA17-05GM bi-polar stepper motor from JOY-IT is driven by a Po-Step25-32 driver to rotate the sample. The motor is connected to the sample via pulley system (ratio 2:5). This increases the steps per resolution to 2590, giving the system more precision and strength to rotate the sample.

5.2 Trigger system

Persistent bubbles are expected to form after the collapse of the cavitation bubble, being caused by the incident laser pulse. The goal of the flow in the channel is to move the persistent bubbles away from the focus spot. To image the persistent bubbles, a shadowgraphy setup is created by placing a LED-pulser powering a Luxeon Rebel Lime LED at one side of the channel and the PixelFly camera at the other side (also see figure 3.10). To keep track of the distance that the bubbles have moved from the laser spot, it is very important to synchronize the laser with the camera and LED. A Thorlabs DET10A/M photo-diode is connected to a BNC 577 pulse generator. The pulse generator is connected to the PixelFly camera and LED-pulser. The photo-diode receives some light from the laser pulse via a BP108 beamsplitter from Thorlabs (92% transmissive and 8% reflective), which is aligned in the beam path (see figure 5.7). The trigger box counts the number of pulses received from the diode and triggers the camera after a predetermined amount of pulses. An extra delay can be set after the predetermined amount of pulses is counted, to change the timing of the camera relative to the laser pulse. The camera needs $5.6\mu s$ to open the shutter. The trigger delay of the LED is set by $5.6\mu s$ after the trigger of the camera. A graphical representation of the trigger system is shown in figure 5.5. For the test in this report, trigger box waits 25 pulses before triggering the LED and camera. After 25 pulses, several persistent bubbles are expected.

5.3 Laser alignment and focus scan

The collimated laser light travels from the laser source over the optical table via some mirrors into the galvo-scanner by Scanlab (see figure 5.7). The diameter of the laser spot in focus was measured to be $35\mu m$. The f-theta lens is mounted on a z-stage, such that the focused spot can be adjusted in the z-direction. If the mirror on the optical table and the z-stage are misaligned, the spot location can shift in the x and y direction if the f-theta lens is moved along the z-axis. To retain a proper alignment a Thorlab BC106-VIS beam profiler was mounted on top of the channel in the spot of the pilot laser. Then

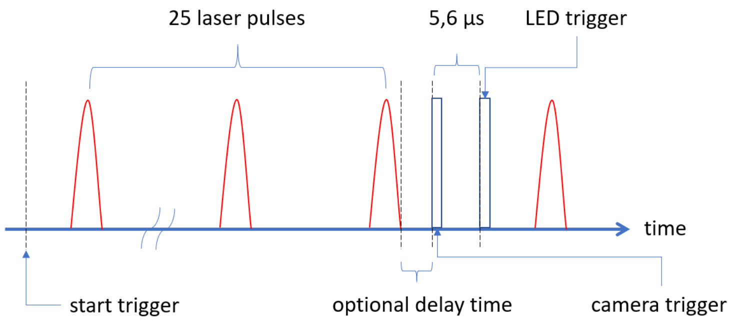

Figure 5.5: A graphical representation of the trigger system.

the z-axis was made to move up and down 100mm around the approximate focus location. The mirrors were adjusted until the shift in the spot was less than $100\mu m$.

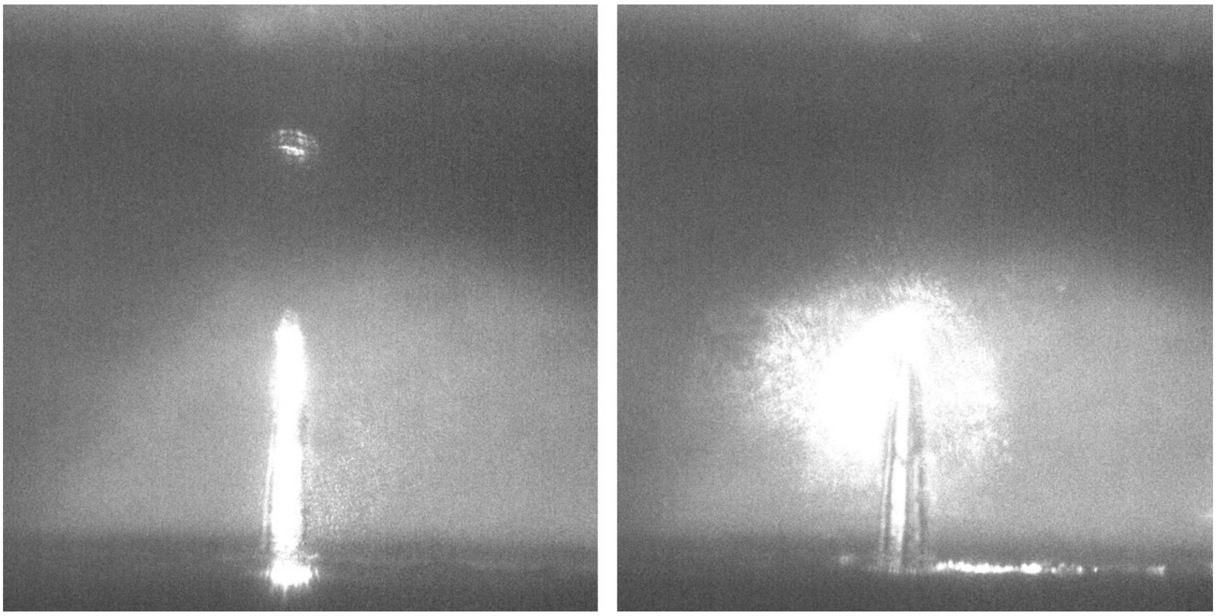

Figure 5.6: The position of the laser relative to the centre of the sample is determined by moving the sample to the pilot laser spot until the pilot laser hits the point of the needle (right image). The laser is in front of the needle in the left image.

A sample with a needle at its centre is used to align the laser in the xy-position. To do this, the pilot laser is turned on and the xy-stages are adjusted until pilot laser lights up the point of the needle as can be seen with the camera from the side (see figure 5.6). The centre of the sample is now determined with an accuracy of 0.5mm (the diameter of the needle). The focus distance is determined by shooting craters on a sample in air around the approximate focus position, changing the z-distance after each crater and moving the channel in the x-direction to shoot a crater at a new location. By looking under a microscope at the craters, the biggest crater can be selected and can be related to a certain z-position of the f-theta lens. The biggest crater indicates that the laser was at the best focus position. The height of f-theta at the focus position needs to compensated by Δz for when there is water in the channel. Δz is determined by equation 5.1 [49]:

$$\Delta z = h(1 - 1/n) \tag{5.1}$$

Using the liquid layer height $h = 5$ and refractive index of water $n = 1.33$, the compensation height can be calculated $\Delta z = 1.24mm$. The focus scan procedure also allowed the determination of how far from the centre the laser could still be shot. This is needed because at some point the laser will not shoot through the laser glass anymore. It turns out that the laser can shoot 8mm from the centre in the x-direction before hitting the glue that was used for the laser glass.

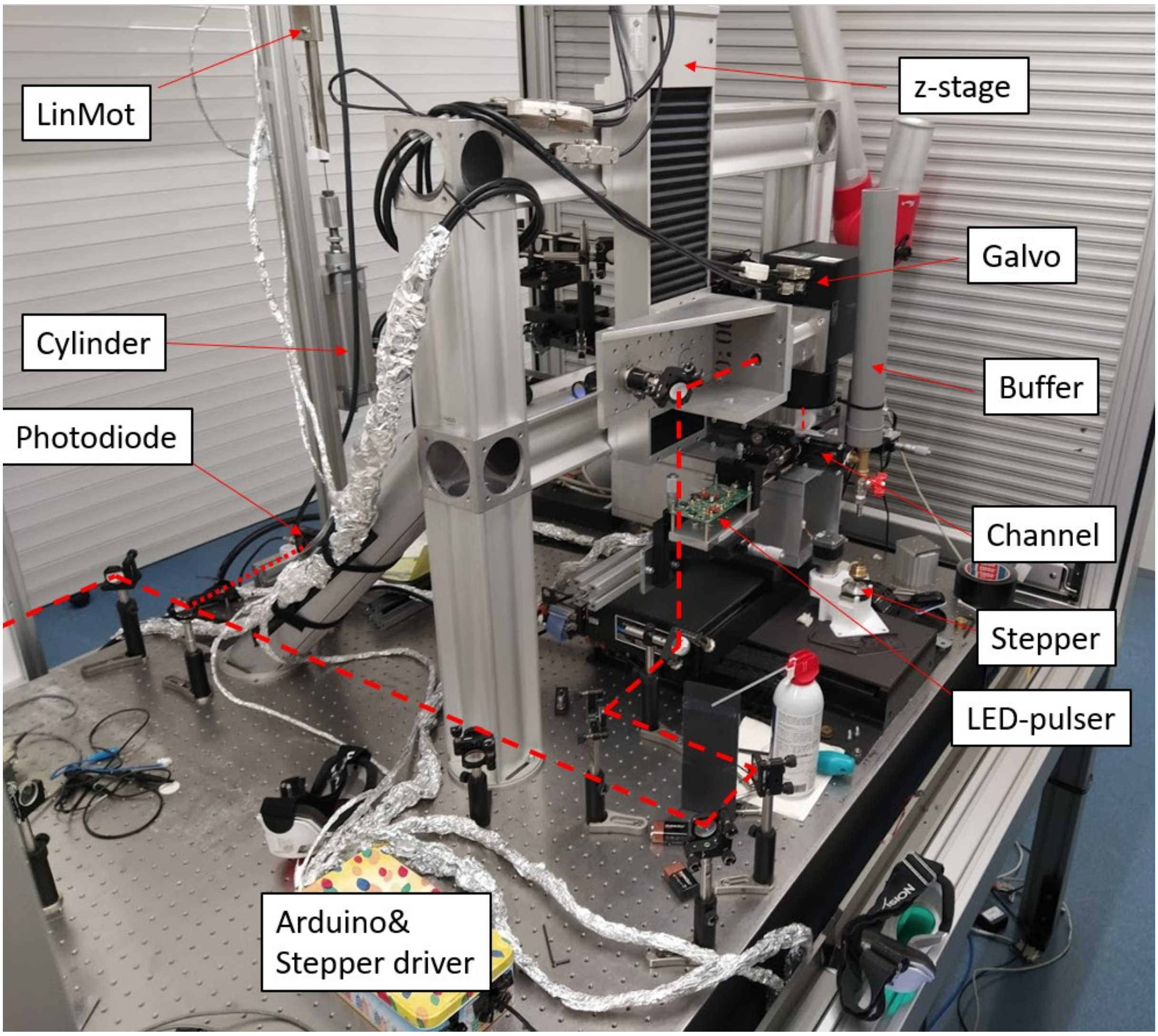

Figure 5.7: An image of the test-setup on the optical table. The laser path is indicated with the red dashed line with a dotted line to the photodiode.

5.4 Test procedure

To start a test run, the channel is filled with water and the cylinder is moved to remove most of the air the system. After removing the air from the system, the laser test can be performed according to the parameters in table 5.2. The selection for the variables of the laser frequency and pulse energy are based on experiences on other test setups with this laser. The Reynolds number are chosen such that there is no flow, a slow laminar flow, a fast laminar flow and a turbulent flow. Five craters per parameter-set are shot. After each set of Five craters, the laser spot is moved over to the FieldMaxII with a $10W$ detector to measure the power of the laser. Then the laser power is adjusted by a $\lambda/2$ plate to the appropriate value. This process is repeated four times for each pulse energy before increasing the frequency. Finally, the flow speed was adjusted. A single trapezoidal velocity profile was used similar to the PIV-measurements, but for the return stroke, a velocity of $0.005m/s$ was chosen to prevent sucking in air via the buffer tank. Unfortunately, the laser glass started leaking a bit after the PIV-tests. To prevent interaction of the laser with water on top of the laser glass, the laser glass is sucked dry with a vacuum cleaner via a 3D printed suction adapter.

Variables:	
Laser frequency	100Hz, 1kHz, 10kHz
Pulse energy	0.155mJ, 0.166mJ, 0.177mJ, 0.188mJ
Reynolds	0, 13, 1953, 6512
Constants:	
Waveform used:	0 (33 ns)
Pulse duration	33ns
Beam Waist diameter:	$35\mu m$
Laser wavelength	1060nm
LED illumination/Camera Shutter	$1\mu s$
LED wavelength	567nm
Pulses per crater	50
Craters per parameter set	5

Table 5.2: The test parameters of the laser test.

When the complete system (see figure 5.1) is set into motion, the following events occur in sequence: The LinMot moves and triggers the limit switch, letting the laser computer know that the flow is fully developed and the first 50 pulses can be shot. The trigger box counts the pulses and triggers the camera and LED to take a picture after the 25th laser pulse. After the 50th pulse, the laser computer sends a command to the Arduino to rotate the sample. Meanwhile, the trigger box is reset manually to start counting pulses again for the next crater. After 5 craters, the power is measured and adjusted. After 20 craters the image sequence (1 image per crater) is saved, the frequency of the laser is adjusted and the sequence starts again. This process is repeated for all the Reynolds numbers.

5.5 Test results

Figure 5.8 shows a compilation of three images at three different frequencies at Reynolds is 0. The red circles indicate the positions of persistent bubbles. There are two more spots visible for the $1kHz$ picture, but they are visible on multiple frames, and are therefore assumed to be bubbles that are stuck to the glass. An extra reflection from the laser is visible in the $1kHz$ and $10kHz$ pictures. Remarkably, the laser spot of the $1kHz$ picture seems to be spread out over a bigger area. This is true for all the pictures at $1kHz$ laser rate, independent of pulse energy, flow rate or position of the spot. So the bubbles at the top of the picture, that are removed with higher flow rates, do not seem to be the cause for the spread of the laser light. Also, the laser light is focused enough to create a cavitation bubble. It is somewhat unexpected to see some laser light on the images of the camera, because the pulse duration of the laser is $33ns$, but the recording of the image starts $5.6\mu s$ later and the shutter closes after $1\mu s$. The next laser pulse will be at least $94\mu s$ later (inter-pulse time of the $10kHz$ frequency is $100\mu s$).

An arrangement of images with Reynolds 13, 1952 and 6523 is shown in figure 5.9. Most notably is the increase in bubble count with higher flow rates. These bubbles were also seen in tests prior to the tests shown in this report before shooting the laser. Initially, the bubbles were suspected to be remaining PIV-particles, but the 'particles' remained after thorough cleaning. Other possible sources, like the construction material of the channel and grease, which was used to seal the side panels, were also tested. Neither the material of the channel nor the grease to seal the channel are the cause of the bubbles. The bubbles seem to be created as a consequence of the cylinder pushing air into the channel. It seems that the cylinder was not vented well enough or the air bubbles are sucked in via the buffer tank. Even at low flow speeds there are bubbles visible that come from an upstream location beyond the

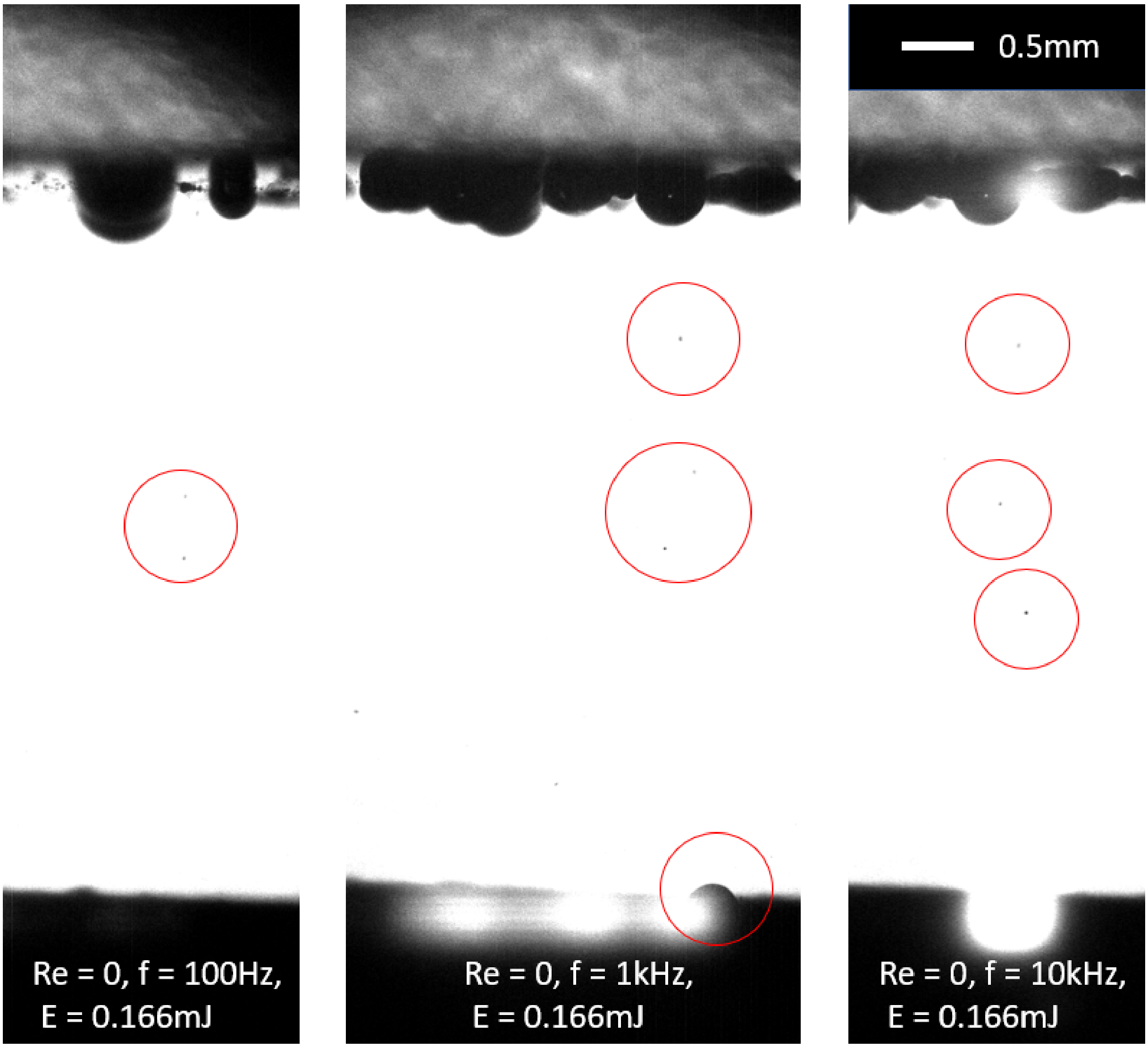

Figure 5.8: Laser tests with stagnant water. The red circles indicate persistent bubbles. On the centre image a cavitation bubble is circled in red.

lasers reach. These bubbles are difficult to distinguish from the persistent bubbles created by the laser. Also, the LED was set too bright, overexposing the images and fading away some detail. Additionally, the LED became less bright throughout the test without manual intervention.

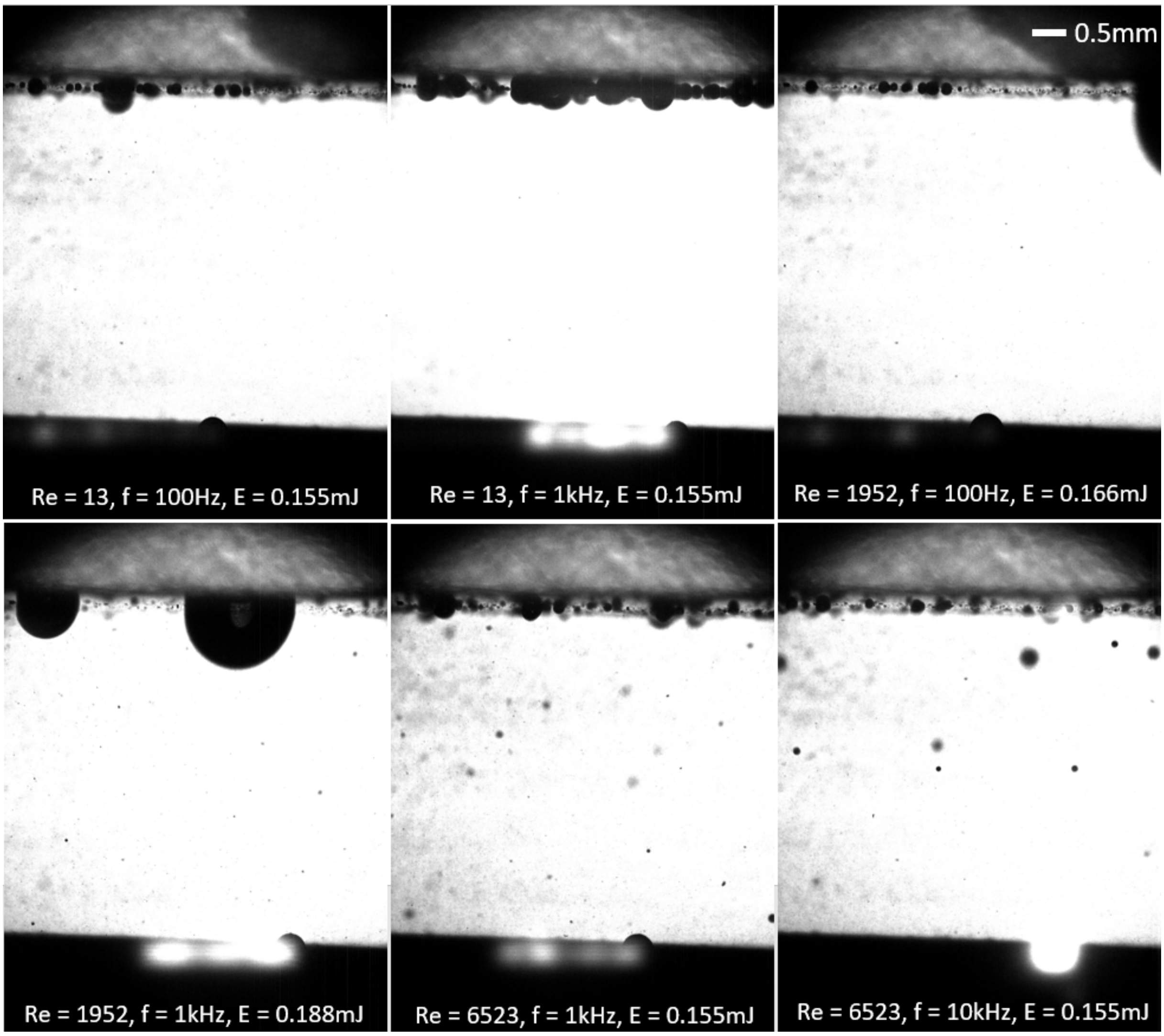

Figure 5.9: An arrangement of images for different flow speeds, pulse energies and laser frequencies.

Chapter 6

Conclusions and recommendations

6.1 Conclusions

A test setup with predictable and repeatable flow condition is made and verified via PIV-measurements. The flow can fully develop in a known velocity profile up to Reynolds 2000, as predicted by theory. For higher Reynolds numbers the velocity profile becomes more rectangular and does not have a parabolic shape anymore. The test setup is tested with a flow rate with a Reynolds number up to 11721, the limit of the hydraulic system. The sample rotation and height adjustment that allows the camera and laser spot to stay at the same position while the sample rotates for a new crater location, works as intended. Thereby allowing the sample to be adjusted to be flush with the channel. The integration of an Arduino with the laser computer is successful, which allows a large part of the experiment to be automated.

Integration of the channel with the laser is also successful. The laser is shot at the sample in the channel, creating cavitation bubbles, persistent bubbles and neatly spaced craters. It is not possible to image the interaction of the liquid flow with the persistent bubbles, as there are too many bubbles in the flow already. These bubbles made it impossible to distinguish between the bubbles created by the laser and the ones that are in the flow already. The bubbles in the flow are a consequence of poor venting of the cylinder, which causes the cylinder to push small bubbles in the channel with each stroke. POM, the material the channel is made from, is not suitable for gluing silica glass to. This causes leaking of liquid from the channel around the laser glass as a consequence.

6.2 Recommendations

The PIV-measurements can be improved by using smaller tracer particles that stay in suspension longer. Better tracers would make the initial push, that is used to get the bigger particles in suspension, unnecessary. This would improve the understanding of how much time it takes to fully develop a flow. Also, the smaller particles would disperse better in the liquid allowing to get more accurate results. Smaller particles require better lighting, which can possibly be achieved by the laser that was used for the ablation process. The infrared laser light was visible on the PixelFly camera. The camera has a relatively good quantum efficiency at the infra-red range and can be upgraded to be suitable for PIV-measurements.

The material for the main body of the channel can be changed to a material that is more suitable for gluing silica glass to, as gluing to POM proved to be really hard and caused leaking around the silica glass. A possible solution would be to redesign the way the silica glass is mounted in the channel. Instead of gluing it in the channel, it can be glued to an metal insert that is screwed in the channel in a similar fashion as the sample (figure 6.1). The silica glass glued very well to the side panels. The side panels are made from PMMA. Making the channel from a different kind of plastic could also be beneficial.

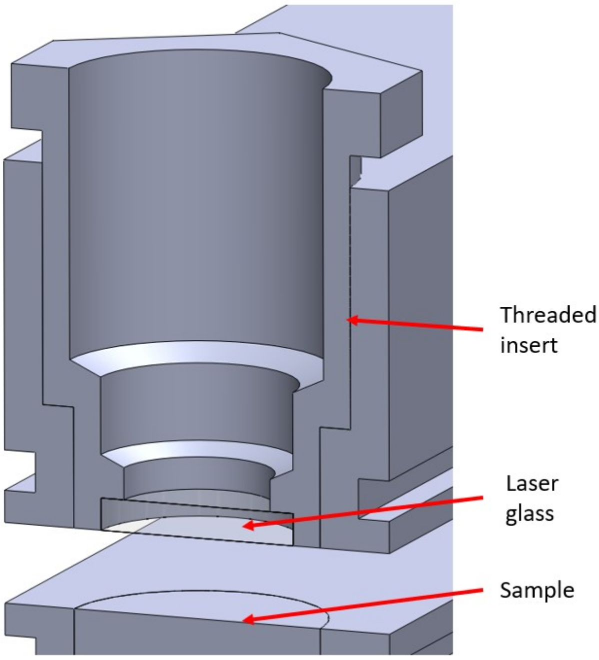

Figure 6.1: A simple representation of a screwable mounting option for the laser glass.

The exact cause for the small bubbles during the laser tests needs to be investigated. A possible cause that can be examined is the venting of the pneumatic cylinder. Maybe there was some trapped air in the cylinder that would be removed with a better positioning of the cylinder, turning the cylinder in such a position that the trapped air cannot get stuck in small crevices. Also, replacing the pneumatic cylinder with a proper hydraulic cylinder can alleviate some of the problems. A hydraulic cylinder would have a longer stroke since there are no dampers at the end of the stroke, as there are with the pneumatic cylinder. An entirely different hydraulic system can be considered as well: a closed circuit design or a gravity system where the liquid can flow from a large tank are possible options.

A high speed camera can dynamically follow the persistent bubbles, making it easier to distinguish laser created bubbles and flow created bubbles (if these are still present in the flow after attempts at improving the hydraulic system). High magnification optics and a high speed camera would allow the imaging of the collapse of the cavitation bubble and the subsequent creation and interaction of the persistent bubbles with a liquid flow.

Bibliography

[1] S. Barcikowski, A. Menéndez-Manjón, and B. N. Chichkov, "Generation of nanoparticle colloids by picosecond and femtosecond laser ablations in liquid flow," vol. 083113, 2012.

[2] A. Kanitz, M. R. Kalus, E. L. Gurevich, A. Ostendorf, S. Barcikowski, and D. Amans, "Review on experimental and theoretical investigations of the early stage, femtoseconds to microseconds processes during laser ablation in liquid-phase for the synthesis of colloidal nanoparticles," *Plasma Sources Science and Technology*, vol. 28, no. 10, 2019.

[3] M. R. Kalus, N. Bärsch, R. Streubel, E. Gökce, S. Barcikowski, and B. Gökce, "How persistent microbubbles shield nanoparticle productivity in laser synthesis of colloids - Quantification of their volume, dwell dynamics, and gas composition," *Physical Chemistry Chemical Physics*, vol. 19, no. 10, pp. 7112–7123, 2017.

[4] T. T. Nguyen, R. Tanabe, and Y. Ito, "Comparative study of the expansion dynamics of laser-driven plasma and shock wave in in-air and underwater ablation regimes," *Optics and Laser Technology*, vol. 100, pp. 21–26, 2018. [Online]. Available: https://doi.org/10.1016/j.optlastec.2017.09.021

[5] D. Kim, B. Oh, and H. Lee, "Effect of liquid film on near-threshold laser ablation of a solid surface," *Applied Surface Science*, vol. 222, no. 1-4, pp. 138–147, 2004.

[6] A. Kanitz, J. S. Hoppius, M. Fiebrandt, P. Awakowicz, C. Esen, A. Ostendorf, and E. L. Gurevich, "Impact of liquid environment on femtosecond laser ablation," *Applied Physics A: Materials Science and Processing*, vol. 123, no. 11, pp. 1–7, 2017.

[7] M. Dell'Aglio, A. De Giacomo, S. Kohsakowski, S. Barcikowski, P. Wagener, and A. Santagata, "Pulsed laser ablation of wire-shaped target in a thin water jet: Effects of plasma features and bubble dynamics on the PLAL process," *Journal of Physics D: Applied Physics*, vol. 50, no. 18, 2017.

[8] H. Seo, J. G. Kim, S. Yoon, and K. Y. Jhang, "Determination of laser beam intensity to maximize amplitude of ultrasound generated in ablation regime via monitoring plasma-induced air-borne sound," *International Journal of Precision Engineering and Manufacturing*, vol. 16, no. 13, pp. 2641–2645, 2015.

[9] C. F. Dowding and J. Lawrence, "Excimer laser machining of bisphenol A polycarbonate under closed immersion filtered water with varying flow velocities and the effects on the etch rate," *Proceedings of the Institution of Mechanical Engineers, Part B: Journal of Engineering Manufacture*, vol. 224, no. 10, pp. 1469–1480, 2010.

[10] C. Y. Liu, X. L. Mao, and E. I. Gyrylov, "Nanosecond Time-Resolved Observations of Laser Ablation of Silver in Water," 2007.

[11] S. M. O. Malley, B. Zinderman, J. Schoeffling, R. Jimenez, J. J. Naddeo, and D. M. Bubb, "Nanosecond laser-induced shock propagation in and above organic liquid and

solid targets," *Chemical Physics Letters*, vol. 615, pp. 30–34, 2014. [Online]. Available: http://dx.doi.org/10.1016/j.cplett.2014.09.061

[12] R. Tanabe, T. T. Nguyen, T. Sugiura, and Y. Ito, "Bubble dynamics in metal nanoparticle formation by laser ablation in liquid studied through high-speed laser stroboscopic videography," *Applied Surface Science*, vol. 351, pp. 327–331, 2015. [Online]. Available: http://dx.doi.org/10.1016/j.apsusc.2015.05.030

[13] T. Tsuji, Y. Tsuboi, N. Kitamura, and M. Tsuji, "Microsecond-resolved imaging of laser ablation at solid-liquid interface: Investigation of formation process of nano-size metal colloids," *Applied Surface Science*, vol. 229, no. 1-4, pp. 365–371, 2004.

[14] S. Ibrahimkutty, P. Wagener, T. D. S. Rolo, D. Karpov, A. Menzel, T. Baumbach, S. Barcikowski, and A. Plech, "A hierarchical view on material formation during pulsed-laser synthesis of nanoparticles in liquid," *Scientific Reports*, vol. 5, pp. 1–11, 2015.

[15] S. Reich, P. Schönfeld, P. Wagener, A. Letzel, S. Ibrahimkutty, B. Gökce, S. Barcikowski, A. Menzel, T. dos Santos Rolo, and A. Plech, "Pulsed laser ablation in liquids: Impact of the bubble dynamics on particle formation," *Journal of Colloid and Interface Science*, vol. 489, pp. 106–113, 2017. [Online]. Available: http://dx.doi.org/10.1016/j.jcis.2016.08.030

[16] L. Shen, Y. Shi, Z. Yang, K. Liu, Y. Wei, and J. Chen, "Investigation of bubble dynamics in different solvents for nanomaterial fabrication by laser ablation in liquid," *EPJ Applied Physics*, vol. 85, no. 3, pp. 1–6, 2019.

[17] T. Tsuji, D. H. Thang, Y. Okazaki, M. Nakanishi, Y. Tsuboi, and M. Tsuji, "Preparation of silver nanoparticles by laser ablation in polyvinylpyrrolidone solutions," *Applied Surface Science*, vol. 254, no. 16, pp. 5224–5230, 2008.

[18] Y. Kawaguchi, "Transient pressure induced by laser ablation of liquid toluene : toward the understanding of laser-induced backside wet etching," vol. 885, pp. 883–885, 2004.

[19] K. Sasaki, T. Nakano, W. Soliman, and N. Takada, "Effect of Pressurization on the Dynamics of a Cavitation Bubble Induced by Liquid-Phase Laser Ablation," pp. 1–4, 2009.

[20] S. Kohsakowski, B. Gökce, R. Tanabe, P. Wagener, A. Plech, Y. Ito, and S. Barcikowski, "Target geometry and rigidity determines laser-induced cavitation bubble transport and nanoparticle productivity-a high-speed videography study," *Physical Chemistry Chemical Physics*, vol. 18, no. 24, pp. 16 585–16 593, 2016.

[21] J. Tomko, S. M. O'Malley, C. Trout, J. J. Naddeo, R. Jimenez, J. C. Griepenburg, W. Soliman, and D. M. Bubb, "Cavitation bubble dynamics and nanoparticle size distributions in laser ablation in liquids," *Colloids and Surfaces A: Physicochemical and Engineering Aspects*, vol. 522, pp. 368–372, 2017. [Online]. Available: http://dx.doi.org/10.1016/j.colsurfa.2017.03.030

[22] T. T. Nguyen, R. Tanabe-Yamagishi, and Y. Ito, "Effects of liquid depth on the expansion and collapse of a hemispherical cavitation bubble induced in nanosecond pulsed laser ablation of a solid in liquid," *Optics and Lasers in Engineering*, vol. 126, no. October 2019, p. 105937, 2020. [Online]. Available: https://doi.org/10.1016/j.optlaseng.2019.105937

[23] S. Zhu, Y. F. Lu, and M. H. Hong, "Laser ablation of solid substrates in a water-confined environment," *Applied Physics Letters*, vol. 79, no. 9, pp. 1396–1398, 2001.

[24] H. W. Kang and A. J. Welch, "Effect of liquid thickness on laser ablation efficiency," *Journal of Applied Physics*, vol. 101, no. 8, 2007.

[25] T. T. Nguyen, R. Tanabe-Yamagishi, and Y. Ito, “Impact of liquid layer thickness on the dynamics of nano- to sub-microsecond phenomena of nanosecond pulsed laser ablation in liquid,” *Applied Surface Science*, vol. 470, no. July 2018, pp. 250–258, 2019. [Online]. Available: https://doi.org/10.1016/j.apsusc.2018.10.160

[26] M. Brikas, S. Barcikowski, B. Chichkov, and G. Račiukaitis, “Production of nanoparticles with high repetition rate picosecond laser,” *Journal of Laser Micro Nanoengineering*, vol. 2, no. 3, pp. 230–233, 2007.

[27] D. Zhang, B. Gökce, S. Sommer, R. Streubel, and S. Barcikowski, “Debris-free rear-side picosecond laser ablation of thin germanium wafers in water with ethanol,” *Applied Surface Science*, vol. 367, pp. 222–230, 2016. [Online]. Available: http://dx.doi.org/10.1016/j.apsusc.2016.01.071

[28] W. Charee, V. Tangwarodomnukun, and C. Dumkum, “Laser ablation of silicon in water under different flow rates,” *International Journal of Advanced Manufacturing Technology*, vol. 78, no. 1-4, pp. 19–29, 2015.

[29] S. Duangwas, V. Tangwarodomnukun, C. Dumkum, S. Duangwas, V. Tangwarodomnukun, and C. Dumkum, “Development of an Overflow-Assisted Underwater Laser Ablation,” vol. 6914, 2014.

[30] T. Wuttisarn, V. Tangwarodomnukun, and C. Dumkum, “Laser micro-milling under a thin and flowing water layer: A new concept of liquid-assisted laser machining process,” *Proceedings of the Institution of Mechanical Engineers, Part B: Journal of Engineering Manufacture*, vol. 230, no. 2, pp. 376–380, 2016.

[31] W. Charee and V. Tangwarodomnukun, “Dynamic features of bubble induced by a nanosecond pulse laser in still and flowing water,” *Optics and Laser Technology*, vol. 100, pp. 230–243, 2018. [Online]. Available: https://doi.org/10.1016/j.optlastec.2017.10.019

[32] Y. K. Madhukar, S. Mullick, and A. K. Nath, “Development of a water-jet assisted laser paint removal process,” *Applied Surface Science*, vol. 286, pp. 192–205, 2013. [Online]. Available: http://dx.doi.org/10.1016/j.apsusc.2013.09.046

[33] O. Tevinpibanphan and V. Tangwarodomnukun, “Effect of Water Flow Direction on Cut Features in the Laser Milling of Titanium Alloy under a Water Layer,” vol. 872, pp. 18–22, 2016.

[34] Y. Ito, “Laser-induced transient stress field studied by time-resolved photoelasticity technique,” *Photon Processing in Microelectronics and Photonics V*, vol. 6106, no. March 2006, p. 61060T, 2006.

[35] T. T. Nguyen, R. Tanabe, and Y. Ito, “Laser-induced shock process in under-liquid regime studied by time-resolved photoelasticity imaging technique,” *Applied Physics Letters*, vol. 102, no. 12, 2013.

[36] P. Gregorčič and J. Možina, “High-speed two-frame shadowgraphy for velocity measurements of laser-induced plasma and shock-wave evolution,” *Optics Letters*, vol. 36, no. 15, p. 2782, 2011.

[37] M. Versluis, “High-speed imaging in fluids,” 2013.

[38] G. Sinibaldi, A. Occhicone, F. Alves Pereira, D. Caprini, L. Marino, F. Michelotti, and C. M. Casciola, “Laser induced cavitation: Plasma generation and breakdown shockwave,” *Physics of Fluids*, vol. 31, no. 10, 2019. [Online]. Available: https://doi.org/10.1063/1.5119794

[39] A. De Bonis, M. Sansone, L. D’Alessio, A. Galasso, A. Santagata, and R. Teghil, “Dynamics of laser-induced bubble and nanoparticles generation during ultra-short laser ablation of Pd in liquid,” *Journal of Physics D: Applied Physics*, vol. 46, no. 44, 2013.

[40] I. Akhatov, O. Lindau, A. Topolnikov, R. Mettin, N. Vakhitova, and W. Lauterborn, “Collapse and rebound of a laser-induced cavitation bubble,” *Physics of Fluids*, vol. 13, no. 10, pp. 2805–2819, 2001.

[41] X. Liu, Y. Hou, X. Liu, J. He, J. Lu, and X. Ni, "Oscillation characteristics of a laser-induced cavitation bubble in water at different temperatures," *Optik*, vol. 122, no. 14, pp. 1254–1257, 2011. [Online]. Available: http://dx.doi.org/10.1016/j.ijleo.2010.08.010

[42] F. White, *Viscous Fluid Flow*, 3rd ed. McGraw-Hill, 2006.

[43] S. van der Linden, R. Hagmeijer, and G. W. Römer, "Picosecond pulsed laser ablation of liquid covered stainless steel: Effect of liquid layer thickness on ablation efficiency," *Journal of Laser Micro Nanoengineering*, vol. 14, no. 1, pp. 108–119, 2019.

[44] Y. S. Muzychka and M. M. Yovanovich, "Pressure Drop in Laminar Developing Flow in Noncircular Ducts : A Scaling and Modeling," vol. 131, no. November 2009, pp. 1–11, 2009.

[45] F. M. White, *Fluid Mechanics 8th Edition*, 2017, vol. 11, no. 3.

[46] N. A. Buchmann, C. E. Willert, and J. Soria, "Pulsed, high-power LED illumination for tomographic particle image velocimetry," *Experiments in Fluids*, vol. 53, no. 5, pp. 1545–1560, 2012.

[47] M. Raffel, C. E. Willert, F. Scarano, C. Kähler, S. Wereley, and J. Kompenhans, *Particle Image Velocimetry*. Springer, 2017.

[48] B. C. Fan and E. Science, "Unsteady , Laminar , Incompressible Flow Through," vol. 16, pp. 351–360, 1965.

[49] A. Menéndez-Manjón, P. Wagener, and S. Barcikowski, "Transfer-matrix method for efficient ablation by pulsed laser ablation and nanoparticle generation in liquids," *Journal of Physical Chemistry C*, vol. 115, no. 12, pp. 5108–5114, 2011.